REPORT DOCUMENTATION PAGE

Form Approved OMB NO. 0704-0188

1. REPORT DATE (DD-MM-YYYY)	2. REPORT TYPE	3. DATES COVERED (From - To)
17-03-2021	Final Report	5-Sep-2018 - 31-Aug-2020

4. TITLE AND SUBTITLE
Final Report: Modular Click Synthesis of Aligned Liquid Crystal Elastomers

5a. CONTRACT NUMBER
W911NF-18-1-0289

5b. GRANT NUMBER

5c. PROGRAM ELEMENT NUMBER
611102

6. AUTHORS

5d. PROJECT NUMBER

5e. TASK NUMBER

5f. WORK UNIT NUMBER

7. PERFORMING ORGANIZATION NAMES AND ADDRESSES
William Marsh Rice University
6100 Main Street

Houston, TX 77005 -1827

8. PERFORMING ORGANIZATION REPORT NUMBER

9. SPONSORING/MONITORING AGENCY NAME(S) AND ADDRESS (ES)
U.S. Army Research Office
P.O. Box 12211
Research Triangle Park, NC 27709-2211

10. SPONSOR/MONITOR'S ACRONYM(S)
ARO

11. SPONSOR/MONITOR'S REPORT NUMBER(S)
69467-CH.3

12. DISTRIBUTION AVAILIBILITY STATEMENT
Approved for public release; distribution is unlimited.

13. SUPPLEMENTARY NOTES
The views, opinions and/or findings contained in this report are those of the author(s) and should not contrued as an official Department of the Army position, policy or decision, unless so designated by other documentation.

14. ABSTRACT

15. SUBJECT TERMS

16. SECURITY CLASSIFICATION OF:			17. LIMITATION OF ABSTRACT	15. NUMBER OF PAGES	19a. NAME OF RESPONSIBLE PERSON
a. REPORT	b. ABSTRACT	c. THIS PAGE			Rafael Verduzco
UU	UU	UU	UU		19b. TELEPHONE NUMBER 713-348-6492

RPPR Final Report
as of 02-Sep-2021

Agency Code: 21XD

Proposal Number: 69467CH **Agreement Number: W911NF-18-1-0289**
INVESTIGATOR(S):

Name: Rafael Verduzco
Email: rafaelv@rice.edu
Phone Number: 7133486492
Principal: Y

Organization: **William Marsh Rice University**
Address: 6100 Main Street, Houston, TX 770051827
Country: USA
DUNS Number: 050299031 EIN: 741109620
Report Date: 30-Nov-2020 Date Received: 17-Mar-2021
Final Report for Period Beginning 05-Sep-2018 and Ending 31-Aug-2020
Title: Modular Click Synthesis of Aligned Liquid Crystal Elastomers
Begin Performance Period: 05-Sep-2018 **End Performance Period:** 31-Aug-2020
Report Term: 0-Other
Submitted By: Rafael Verduzco Email: rafaelv@rice.edu
Phone: (713) 348-6492

STEM Degrees: **STEM Participants:** 3

Major Goals: The overarching objective of the proposed work is to quantify the relationship between network structure and mechanical properties in liquid crystal elastomers (LCEs). Liquid crystal elastomers (LCEs) are shape-responsive materials that combine the elastic properties of a polymer network with the molecular ordering and responsiveness of liquid crystals. The combination of network elasticity, low crosslink density, and liquid crystal ordering results in versatile shape-responsive materials. LCEs have significant potential for biomedical applications, sensors, artificial robots and devices, micro-actuators, responsive surface coatings, and other applications.

The shape-responsiveness and unique mechanical properties of LCEs arise from coupling of liquid crystal ordering to an elastic polymer network. The most popular approach for preparing LCEs involves the use of poly(siloxane) chains and hydrosilylation reactions for functionalizing and crosslinking. This network chemistry approach does not enable control over the shape or crosslink density of the LCE. Recent work has demonstrated that LCEs can be prepared rapidly and with better control over network structure through click chemistries, including thiol-ene click chemistries.

Our proposed work will specifically address the mechanical properties of LCEs prepared through thiol-ene click coupling. The use of thiol-ene click coupling has enables the scalable fabrication of LCEs with a non-planar shape. Our work will address the role of soft elasticity in these networks and the impact on shape responsiveness.

Specific Objectives include:
Task 1: Optimize the double network crosslink density, linker length, and phase behavior to achieve mechanically shape-programmable LCEs. In this task we will seek to mechanically program complex 3-D shapes in LCEs. Prior work has produced aligned LCEs through uniaxial extension, but the resulting materials can undergo relatively simple shape changes (extension/contraction). Recent work has also demonstrated surface patterning of liquid crystals to produce more complex shapes, but this is limited to thin films. Our work will demonstrate more general, non-planar, three-dimensional shape changes in LCEs.

Task 1.1: Quantify the role of network chemistry on shape programming. In preliminary work, we have demonstrated that the composition of the double network LCEs has a strong impact on the shape reversibility of LCEs (Figure 2). We quantified the ability of an LCE to return to a flat programmed shape and demonstrated this was a strong function of the crosslink densities of the first and second network. This arises due to competition between the first and second polymer networks. We will systematically investigate the role of crosslink density, linker length, and liquid crystal phase behavior on shape-responsiveness. The Tg and TNI will be tuned using linkers of varying length and composition. We will measure the ability of LCEs to hold an arbitrary, non-planar

shape and to return to the initially programmed shape.

Task 1.2: Pattern micron-scale features in shape-responsive LCEs. To date mechanical deformations have been applied to produce LCEs capable of bulk shape changes. With the optimized network chemistry, we will explore the preparation of micron and sub-micron sized patterns and features that can be actuated through heat or light. The fidelity of the patterned feature and actuation will be quantified through optical profilometry.

Task 1.3: Optimize light-actuated response in LCEs. In this task we will explore light-actuation as a general approach to produce arbitrary patterns and shape-changes in mechanically-programmed LCEs.

Task 2: Quantify the role of network structure and chemistry on soft elastic response. LCEs exhibit a soft-elastic plateau during deformation due to rotation of the liquid crystal director which accommodates shape change. However, to date a systematic study of how network structure influences soft elastic response has not been carried out.

Task 2.1: Examine the role of double network structure on soft elasticity. LCEs are commonly made through a two-step crosslinking method, resulting in two interpenetrating and competing networks. The soft elastic response in LCEs has focused primarily on polydomain, single-network materials. Here, we will carry out systematic studies to quantify the role of double network structure – including crosslink densities and relative alignment – on the soft elastic response. Characterization will involve stress-strain, compression, and indentation measurement.

Task 2.2: Characterize the role of liquid crystal content and phase on soft elasticity. We will characterize the soft elastic response in a series of LCEs with varying liquid crystal content and with both smectic and nematic phases.

Task 2.3: Understand the role of network genesis on soft elasticity. LCEs can be synthesized under isotropic or liquid crystal phases, resulting in isotropic and nematic genesis networks. We will characterize the impact of network genesis on the soft elastic response of thiol-ene LCEs.

Task 2.4: Compare the mechanical behavior of mechanically and surface-programmed LCEs. LCEs can be aligned using surfaces (which align the liquid crystal director) or through mechanical strain (which deforms the network to align the liquid crystal director). We will carry out a direct comparison of the mechanical responses of LCEs synthesized using these two techniques to understand the resulting mechanical behavior and soft elastic response.

Accomplishments: Our work focused on bulk LCE samples and LCEs produced through additive manufacturing. We produced a publication on each of these topics.

In studies of bulk LCEs, we demonstrated that LCEs are double-network materials. This is an important concept for shape programming because it emphasizes that LCEs have two competing polymer networks. LCEs are typically made using a two-step crosslinking process, and in order to optimize the shape-responsiveness, we need to optimize the balance of the crosslink densities of the two networks. We used thiol-ene chemistry to systematically tailor the crosslink densities of the first and second networks. This chemistry enabled us to independently control the network crosslink densities and demonstrate that shape responsiveness and fixity could be optimized by achieving an optimal balance of these two networks. Using the optimal network chemistry, we next demonstrated that a variety of shapes could be programmed, including flat, non-planar, and samples with features imprinted on the surface.

One drawback of bulk LCE synthesis methods is that it is difficult to achieve more complex architectures. In a second major study, we developed a novel LCE synthesis method using additive manufacturing. Our approach involved producing an oligomeric liquid crystal mixture that could be printed into a solvent bath. The oligomeric mixture was crosslinked during printing, enabling us to produce fibers of different shape and size. Next, we demonstrated that we could recover the fibers, dry them, and shape program them. This LCE synthesis approach therefore provides the advantages of additive manufacturing in producing a sophisticated architecture along with the simplicity of mechanical shape deformation for shape programming. We characterized the mechanical properties of printed fibers and scaffolds, and found comparable properties to bulk LCEs.

In a supplementary project funded by an HRAP and URAP supplement, we looked at light-activated shape changes in LCEs. We specifically focused on the fabrication of micropumps based on LCEs for lab-on-a-chip applications. The project mentored two students, one undergraduate and one high school, and the students worked on the fabrication and characterization of an LCE micropump over the course of a summer. These students were

successful in demonstrating a proof-of-principle LCE micropump. Their specific contributions were in the development of novel processing approaches and the development of light-responsive LCEs.

Altogether, work under this project provided novel insight into the mechanical properties and processing of LCEs.

Training Opportunities: The project supported graduate student Morgan Barnes. Morgan produced two first-author publications and will graduate this year. She has accepted a postdoctoral position at Cambridge University which will begin this summer.

The project also mentored Shaan Parekh and Sueda Cetinkaya. Sueda is graduating this year and will pursue a PhD. Shaan is currently an undergraduate student.

Results Dissemination: Two publications were produced under this project.

The work was presented at a number of university presentations and conferences:

1. Verduzco presented the work at the 2019 International Liquid Crystal Elastomers Conference
2. Morgan Barnes presented work on 4D printing at the 2019 International Liquid Crystal Elastomers Conference.
3. Verduzco presented the work as part of invited department seminars at the University of Southern Mississippi, Carnegie Mellon, and the University of Akron

Honors and Awards: Morgan Barnes received the Best Student Presentation Award at the 2019 International Liquid Crystal Elastomers Conference for her presentation of this work.

Protocol Activity Status:

Technology Transfer: Nothing to Report

PARTICIPANTS:

Participant Type: Graduate Student (research assistant)
Participant: Morgan G Barnes
Person Months Worked: 15.00 **Funding Support:**
Project Contribution:
National Academy Member: N

Participant Type: Graduate Student (research assistant)
Participant: Morgan G Barnes
Person Months Worked: 15.00 **Funding Support:**
Project Contribution:
National Academy Member: N

Participant Type: PD/PI
Participant: Rafael Verduzco
Person Months Worked: 15.00 **Funding Support:**
Project Contribution:
National Academy Member: N

Participant Type: Undergraduate Student
Participant: Sueda Cetinkaya
Person Months Worked: 5.00 **Funding Support:**
Project Contribution:

RPPR Final Report
as of 02-Sep-2021

National Academy Member: N

Participant Type: High School Student
Participant: Shaan Parekh
Person Months Worked: 5.00 **Funding Support:**
Project Contribution:
National Academy Member: N

ARTICLES:

Publication Type: Journal Article Peer Reviewed: Y **Publication Status:** 1-Published
Journal: Soft Matter
Publication Identifier Type: DOI Publication Identifier: 10.1039/C8SM02174K
Volume: 15 Issue: 5 First Page #: 870
Date Submitted: 6/18/19 12:00AM Date Published:
Publication Location:
Article Title: Direct shape programming of liquid crystal elastomers
Authors: Morgan Barnes, Rafael Verduzco
Keywords: liquid crystal elastomers, shape programming
Abstract: Liquid crystal elastomers (LCEs) are shape morphing materials promising for many applications including soft robotics, actuators, and biomedical devices, but current LCE synthesis techniques lack a simple method to program new and arbitrary shape changes. Here, we demonstrate a straightforward method to directly program complex, reversible, non-planar shape changes in nematic LCEs. We utilize a double network synthesis process that results in a competitive double network LCE. By optimizing the crosslink densities of the first and second network we can mechanically program non-planar shapes with strains between 4–100%. This enables us to directly program LCEs using mechanical deformations that impart low or high strains in the LCE including stamping, curling, stretching and embossing methods. The resulting LCEs reversibly shape-shift between the initial and programmed shape. This work widens the potential application of LCEs in biomedical devices, soft-robotics and micro-fluidics where
Distribution Statement: 3-Distribution authorized to U.S. Government Agencies and their contractors
Acknowledged Federal Support: **Y**

Partners

,

RPPR Final Report
as of 02-Sep-2021

I certify that the information in the report is complete and accurate:
Signature:
Signature Date:


Sueda Cetinkaya
Morgan Barnes
Shaan Parekh

Soft Matter

PAPER

View Article Online
View Journal | View Issue

Cite this: *Soft Matter*, 2019, **15**, 870

Direct shape programming of liquid crystal elastomers†

Morgan Barnes [a] and Rafael Verduzco *[ab]

Liquid crystal elastomers (LCEs) are shape morphing materials promising for many applications including soft robotics, actuators, and biomedical devices, but current LCE synthesis techniques lack a simple method to program new and arbitrary shape changes. Here, we demonstrate a straightforward method to directly program complex, reversible, non-planar shape changes in nematic LCEs. We utilize a double network synthesis process that results in a competitive double network LCE. By optimizing the crosslink densities of the first and second network we can mechanically program non-planar shapes with strains between 4–100%. This enables us to directly program LCEs using mechanical deformations that impart low or high strains in the LCE including stamping, curling, stretching and embossing methods. The resulting LCEs reversibly shape-shift between the initial and programmed shape. This work widens the potential application of LCEs in biomedical devices, soft-robotics and micro-fluidics where arbitrary and easily programmed shapes are needed.

Received 25th October 2018,
Accepted 12th December 2018

DOI: 10.1039/c8sm02174k

rsc.li/soft-matter-journal

1. Introduction

Liquid crystal elastomers (LCEs) are polymeric networks that exhibit large and reversible shape changes in response to a variety of stimuli including heat, UV or near-IR light and magnetic or electric fields.[1–8] These materials are promising as actuators and for applications in soft robotics.[9–25] However, current synthesis and processing methods limit the fabrication of LCEs with complex, arbitrary shape changes.

LCE shape changes are governed by a coupling between the liquid crystal director and the anisotropic polymer network. Monodomain nematic LCEs with a uniform alignment of the liquid crystal director can be prepared *via* uniaxial mechanical extension during synthesis. By heating the sample beyond the nematic-to-isotropic transition temperature T_{NI}, the system transitions from the state programmed in the nematic phase to that programmed in the isotropic state.[26–28] Such monodomain LCEs reversibly change shape with heating and cooling due to changes in the liquid crystal order parameter, which is coupled to the network anisotropy.[29] Contraction and elongation, curling, and surface wrinkling have been reported using mechanically aligned monodomain LCEs and LCE bilayers.[4,30–33]

More diverse shape changes in LCEs can be achieved by imprinting complex nematic director orientations. For example, elaborate director orientations and liquid crystal images can be imprinted into LCEs using patterned surfaces to produce a range of shape responses including splay, conical structures, and Gaussian curvatures.[6,34–43] Additive manufacturing has also been recently employed to produce LCEs that can transition between two non-planar shapes.[44,45] A complication of these methods is that they generally require solving the inverse problem of determining the necessary liquid crystal director profile to produce a desired shape change.[41,46–48] Further, the use of patterned surfaces relies on surface forces, limiting the technique to thin, flat samples. Other approaches include simultaneously stretching the LCE in different directions to mechanically align a specific director profile[49] or curling and crosslinking a stretched monodomain LCE.[50] The approach of curling and crosslinking a monodomain LCE opens up a method for arbitrarily programming curvatures in LCEs with some limitations in the strain range possible and necessity for starting with a uniaxially oriented LCE.[50]

Here we investigate an alternative and straightforward method to program complex three-dimensional shapes in nematic LCEs by mechanically deforming the LCE into a desired non-planar shape during a double network synthesis process, as shown in Fig. 1. The resulting LCE should reversibly transition between the shapes programmed during the first and second network crosslinking reactions. A challenge of implementing this approach is that non-planar mechanical deformations such as curling produces low (<10%) strains, while stretching produces much larger (100%) strains. The LCE network chemistry should be optimized to be able to lock-in deformations over this entire strain range.

[a] *Department of Materials Science and NanoEngineering, Rice University, Houston, Texas 77005, USA. E-mail: RafaelV@Rice.edu*
[b] *Department of Chemical and Biomolecular Engineering, Rice University, Houston, Texas 77005, USA*

† Electronic supplementary information (ESI) available. See DOI: 10.1039/c8sm02174k

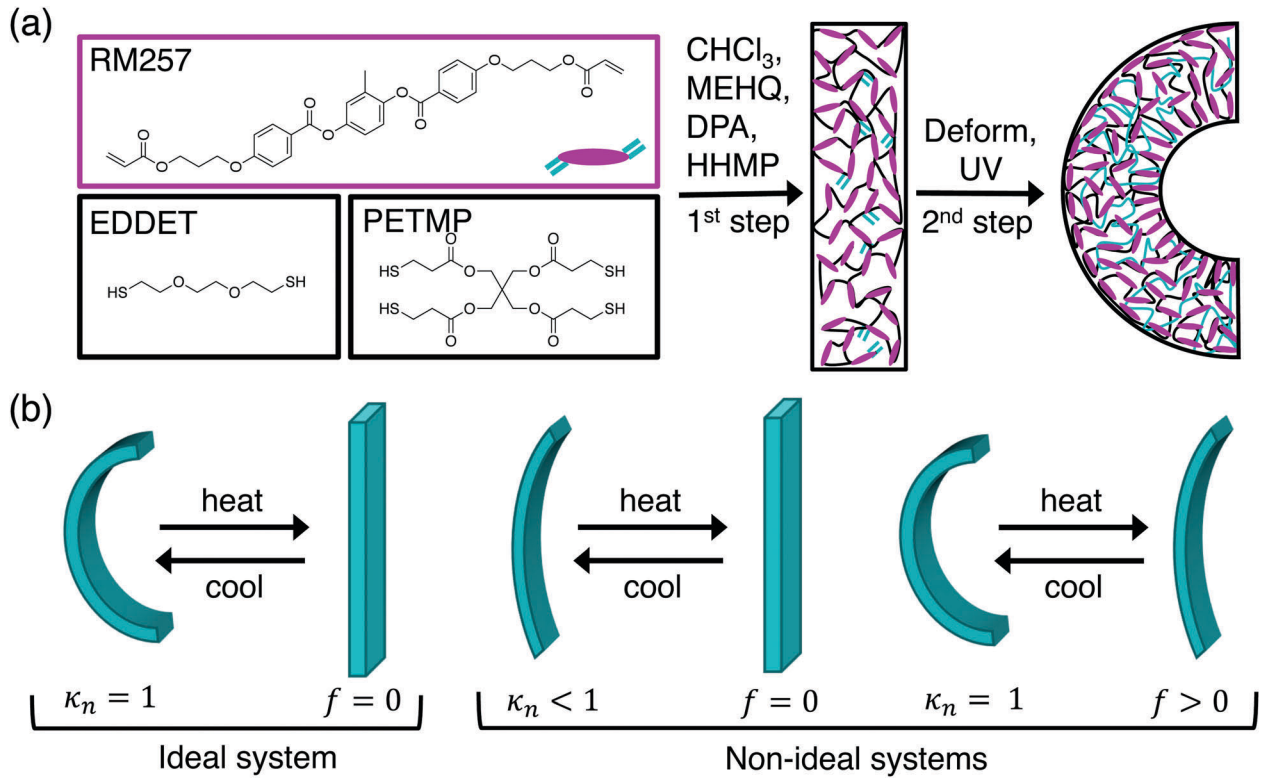

Fig. 1 (a) Schematic for the preparation of LCEs including the resulting liquid crystal alignment. The curvature causes parallel alignment of the liquid crystals at the outer edge due to tensile forces. Perpendicular alignment occurs at the inner edge due to compressive forces and could either be in plane, as depicted, or into the page. (b) Schematic illustrating the ideal and non-ideal shape changes of fully cured LCEs and their respective normalized curvature, κ_n, and flatness, f values.

The concept of a competitive double network structure is useful to guide optimization of the LCE to achieve reversible shape programming. In a typical LCE synthesis, the first network is cured in the isotropic state, deformed by mechanically loading the sample, and then cured again in the nematic state. LCEs fabricated using this general approach are an example of double network elastomers, which have been studied for over 50 years.[51–55] A general feature of double network elastomers is that the final state of the dual-cure elastomer retains some fraction of the strain applied during the second crosslinking reaction and is dependent on the relative crosslink densities or moduli of the first and second network crosslinking reactions.[56,57] This concept of a double network structure has also been applied to double network shape memory polymers where the elastic restoring force of the first network must be balanced with the strength of the second network to enable reversible[58] and irreversible shape changes.[59,60]

In the case of a double network LCE, we hypothesized that finding the proper balance between the first and second networks would be necessary to achieve reversible shape programming compatible with a wide range of sample strains. Below, we demonstrate optimization of the LCE network composition by systematically varying the network composition of the first and second crosslinking steps to produce LCEs that can transition between a mechanically programmed bend deformation and fully recover their initial shape on heating. We show that the resulting optimized LCE can be used to mechanically program shapes with strains in the range of 4–100%, and we demonstrate programming and reversible shape changes using curling, stamping, stretching, and embossing methods. This method necessitates no foresight of the required director profile and is not limited to initially flat films. The resulting LCEs can shape-morph between three-dimensional topologies and reproduce shapes and textures with low- and high-strain deformations.

The demonstrated method of mechanically deforming a material to produce a desired shape change is similar to those commonly used to program shape memory polymers (SMPs). In a SMP a temporary shape is directly imprinted in a polymer at elevated temperatures and remains after the materials is quenched.[61–63] When the SMP is heated the original shape is recovered and the programmed shape is generally lost unless it is reprogrammed. Our work combines the straightforward shape-programming in SMPs with the full shape-reversibility of LCEs.

2. Experimental methods

2.1. Materials and methods

2,2′-(Ethylenedioxy) diethanethiol (EDDET), pentaerythritol tetrakis (3-mercaptopropionate) (PETMP), 1,4-bis-[4-(3-acryloyloxypropyloxy)benzoyloxy]-2-methylbenzene (RM257), chloroform, dipropyl amine (DPA), 4-methoxyphenol (MEHQ), and (2-hydroxyethoxy)-2-methylpropiophenone (HHMP) were obtained from commercial suppliers and used as received.

2.2. Synthesis

LCEs are made following a previously reported double network thiol-acrylate polymerization.[28] RM257 is the liquid crystal monomer and is a chain extender for the first network and the crosslinker in the second network. EDDET and PETMP act as flexible chain extenders and crosslinkers for the first network, respectively. A series of LCEs that varied in PETMP and excess acrylate contents were prepared using the same general procedure. The following procedure is for an LCE with 10 mol% excess acrylate and 25 mol% of the thiols coming from PETMP. First, RM257 (300 mg, 0.510 mmol), 0.5 wt% HHMP (1.5 mg), and 0.25 wt% MEHQ (0.75 mg) are dissolved in chloroform (120 mg) at 70 °C. MEHQ is added to prevent unintentional acrylate–acrylate polymerization before UV-curing. After the mixture has cooled to room temperature EDDET (63.31 mg, 0.348 mmol) and PETMP (28.29 mg, 0.058 mmol) are added followed by a 2 wt% DPA solution in chloroform (46.26 mg, 0.009 mmol, 1 mol%). The masses of reagents used to synthesize other compositions are listed in Table S1 (ESI†) and the chemical reaction scheme is reported in Scheme S1 (ESI†). The mixture is then vortexed to ensure proper mixing and placed under vacuum to remove any bubbles. Next, the mixture is deposited into the desired mold and cured for at least 5 hours. After the first cure is complete the LCE is heated to 80 °C under a vacuum of 30 mmHg for 5 hours to remove the chloroform. Finally, the LCE is mechanically deformed to the desired shape and irradiated with 365 nm light for 10 minutes to complete the second cure step. Additional details on the molds used for the first cure step and methods for deforming the LCEs during the second cure step are included below.

2.3. Imaging and image analysis

Cross-polarized optical images were taken using a Zeiss Axioplan 2 microscope. A curved LCE was imaged through its thickness with the polarizers at 0 and 45 angles from the outer edge. The gray scale images were subtracted from each other to obtain the intensity change image. All three images were then mapped to the same color scale to illustrate intensity differences.

Programmed LCEs were imaged using an iPhone camera with the color levels adjusted to enhance contrast with the background. Python and OpenCV were used for all image analysis. To determine normalized curvature and flatness, blackened samples were imaged against a white background at room temperature. A circle was fitted to the outer edge of the digital sample image, and the normalized curvature κ_n was calculated using eqn (1),

$$\kappa_n = \frac{\rho_{cure} + t}{\rho_{LCE}} \quad (1)$$

where ρ_{LCE} is the radius of curvature of the LCEs outer edge, ρ_{cure} is the radius of curvature of the rod used in the second cure, and t is the thickness of the LCE.

To calculate flatness, the samples were imaged at 150 °C, which is well above the T_{NI} for all samples. A line was fitted to the midpoint between the detected edges of the digital image, and a standard error was calculated to determine flatness f using eqn (2),

$$f = \sqrt{\frac{\sum (Y - Y')^2}{N}} \quad (2)$$

where Y is the mean value of the LCEs outer and inner edges at a specific position, Y' is the fitted line value at that position, and N is the number of position sampled along the sample length.

2.4. Two-dimensional wide angle X-ray scattering (WAXS)

Liquid crystal orientation and order parameter were calculated using a Rigaku diffractometer using a RUH3R Copper Target Rotating Anode with a wavelength of 0.154 nm, phi axis goniometer with vertical orientation, and a Rigaku R-Axis IV++Image Plate Area Detector. The detector imaging area is approximately 380 mm × 380 mm, with a distance of 300 mm between the sample and detector. The order parameter was calculated numerically with Python using eqn (3) from Deutsch *et al.*[64,65]

$$S = 1 - N^{-1}\frac{3}{2}\int I(\theta)\left[\sin^2\theta + \left(\sin\theta\cos^2\theta\right)\log\left(\frac{1+\sin\theta}{\cos\theta}\right)\right]d\theta \quad (3)$$

where $N = \int I(\theta)d\theta$.

2.5. Differential scanning calorimetry

The glass transition, T_g, and nematic to isotropic transition temperature, T_{NI}, were determined using TA instruments Q20 differential scanning colorimeter (DSC). LCEs were analyzed prior to the second curing step because the T_{NI} is not detectable by DSC after the second cure step.[28] Samples were equilibrated to −20 °C for 5 minutes and then heated at a rate of 5 °C min^{-1} to 100°, held at that temperature and for 5 minutes and then cooled to −20 °C at a rate of 5 °C min^{-1}. The cycle was repeated once more and T_g and T_{NI} were determined from the second heating cycle as the stepwise decline and endothermic well in the heat flow, respectively.

2.6. Dynamic mechanical analysis

Young's moduli were obtained using an ARES G2 (TA instruments) rheometer using a linear film tension clamp. Rectangular samples were loaded into the clamp and pulled at a Hencky strain rate of 5% min^{-1}. Young's modulus is calculated as the slope of a line fitted to the stress–strain curve from 0 to 1.5% strain.

2.7. Actuation and fixity

Fixity and actuation were determined by first placing two marks a distance of 10 mm apart on a rectangular LCE that has undergone the first network crosslinking reaction. The length of the sample at this stage is denoted the initial length l_0. The sample was then stretched to a desired strain (*e.g.*, 20 mm for 100% cure strain), UV cured for 10 minutes, heated above the T_{NI}, and then cooled back to room temperature.

The distance between the marks was measured in both the elongated state (room temperature) and contracted state

(above T_{NI}) to determine the elongation and contraction fixities. Elongation fixity is the ratio of the elongated length, l_e, to the cured length, l_{cure}, and contraction fixity is the ratio of the contracted length, l_c to the initial length, l_0. The actuation strain, $\varepsilon_{actuation}$, and normalized actuation strain, $\varepsilon_{normalized}$, were calculated using eqn (4) and (5),

$$\varepsilon_{actuation} = \frac{l_e - l_c}{l_c} \times 100 \quad (4)$$

$$\varepsilon_{normalized} = \varepsilon_{actuation} \times \frac{l_0}{l_{cure} - l_0} \times 100 \quad (5)$$

where $\varepsilon_{normalized}$ is $\varepsilon_{actuation}$ normalized by the cure strain.

2.8. LCE programming

All fabrication molds and stamps can be found in the Fig. S1 (ESI†). The LCE face, four pillar structure, and Rice logo were all fabricated using an embossing method. LCEs were initially cured between two glass slides with spacers to yield a desired thickness. The LCE was then pressed between a positive and negative mold of the same object, placed in a freezer for 10 minutes to prevent sticking to the mold, removed from the mold and cured for 10 minutes under 365 nm UV light.

The face was made using a purchased silicone mold of the negative face, and the positive image was created from pressing Sculpey oven bake clay into the silicone cavity. The clay was then baked 15 minutes at 130 °C for every 1/4 inch of thickness. The four-pillar structure was fabricated in a similar fashion, with a LEGO® piece as the positive image and the pressed clay as the negative.

The Rice logo was created using a Universal X-660 laser cutter. The logo was cut into 3/32 inch-thick basswood. The positive and negative logos were glued onto basswood substrates to create the positive/negative stamps.

The wave LCE was made using a polydimethylsiloxane (PDMS) mold. First, clay was flattened to uniform thickness (1 mm) and hand curved into a wave structure. The clay was placed upright in a plastic container and uncured PDMS was poured around the clay and cured at room temperature for 24 hours. Then the PDMS was removed from the container, cut in half, and the clay was removed. The PDMS mold was placed back in the container, and LCE solution was poured into the cavity and cured, removed, and dried. The wave LCE was then flattened, curled around a rod, and UV cured.

The quarter LCE was made by lightly hand pressing an initially flat LCE against the back surface of a quarter. The LCE was then removed from the quarter and UV cured. The flower was made by cutting a petaled spiral out of a, initially flat LCE and hand rolling it into a flower and UV cured. Additional programmed LCEs are shown in the Fig. S2 (ESI†).

3. Results and discussion

Our first objective was to optimize the LCE network composition by quantifying the ability of an LCE to hold a curled shape and reversibly transform to a flat sheet, as illustrated in Fig. 1. Ideally, the LCE should fully and reversibly transition between the flat and curled shapes, as shown schematically in Fig. 1b. We hypothesized that this could be achieved by optimizing the compositions of the first and second network.

Table 1 Compositions and thermal properties of LCE samples prepared. PETMP Thiol content is the mol% of thiol functional groups from PETMP, and excess acrylate is the mol% excess of acrylate functional end groups relative to thiol functionalities. T_g and T_{NI} determined using differential scanning calorimetry

PETMP thiol content (%)	Excess acrylate (%)	T_g (°C)	T_{NI} (°C)
10	5	1.93	84.21
	10	−0.27	83.52
20	5	0.33	79.90
	10	−1.89	79.33
	15	−1.82	81.40
25	5	2.39	85.10
	10	0.49	79.64
	15	2.35	86.73
40	5	6.5	78.21
	15	3.98	84.78
	25	−1.23	86.26
60	5	11.62	80.12
	15	8.86	90.11
	25	4.18	89.62
80	5	14.95	91.09
	15	16.2	91.21
	25	8.94	87.65

The double network chemistry chosen to prepare LCEs enables systematic modulation of the crosslink densities of the first and second networks through variation of the PETMP content and relative excess of the acrylate functional groups to thiols. The PETMP content determines the degree of branching and crosslinking in the first network while the excess acrylate content influences the crosslink densities of both the first and second networks. The network composition has only a modest impact on the glass-transition temperature, T_g, and nematic-to-isotropic transition temperature, T_{NI}, as shown in Table 1. The T_g increases with PETMP content, and T_{NI} is not greatly affected by these variations in network composition. This is consistent with prior studies of similar LCE networks.[66]

As shown in Fig. 2a, the modulus of LCEs always increases between the first and second crosslinking steps, as expected. Also, increasing the PETMP content generally increases the final modulus after both network crosslinking steps. This is expected because a higher PETMP content increases network branching and crosslink density. Finally, increasing the excess acrylate content decreases the modulus of the first network and increases the modulus of the second network, producing a much larger jump in modulus between first and second crosslinking steps at higher acrylate contents.

To quantify the ability of the LCEs to hold a programmed curvature and return to a flat sheet when heated above T_{NI}, an initially flat polydomain LCE was wrapped around a rod with a known radius of curvature and photo-cured to define the

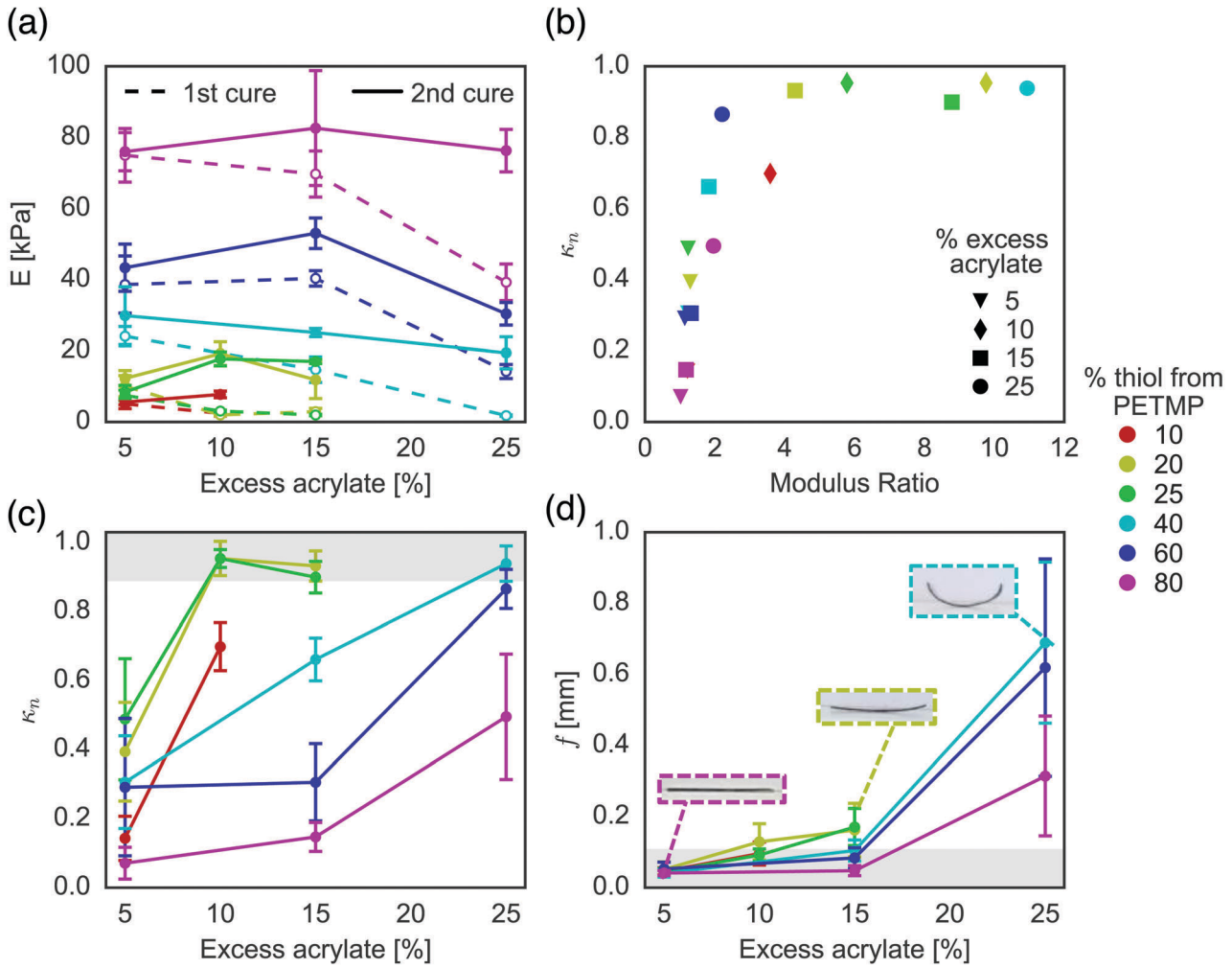

Fig. 2 (a) LCE Young's moduli after the first and second network crosslinking reactions (n = 3, error bars indicate 95% confidence intervals of the mean). (b) The mean normalized curvature, κ_n as a function of the ratio of Young's moduli after the 2nd cure relative to the 1st cure. (c and d) Normalized curvature, κ_n, and fatness, f, of LCEs ($t \approx 250$ μm) photo-cured around a rod (ρ = 2.455 mm). Grey regions indicate samples that maintain their programmed curvature at room temperature and flatten when heated (n = 15, error bars indicate 95% confidence intervals of the mean). Numerical data is reported in Table S2 (ESI†).

second network and lock-in the curled shape. Residual stresses were then removed by subjecting each sample to one heating and cooling cycle above T_{NI} ($\approx$75–90 °C). We then measured the normalized curvature κ_n and flatness parameter f for each sample. The normalized curvature κ_n is the ratio of the programmed to actual radius of curvature at room temperature. The flatness parameter f is the standard error for a linear fit to a cross-sectional image of the LCE at temperatures above T_{NI}. Details on the measurement and determination of κ_n and f are provided in the Experimental section. In the ideal scenario where an LCE holds the programmed curvature at room temperature and returns to a perfectly flat sheet on heating above T_{NI}, $\kappa_n = 1$ and $f = 0$.

As shown in Fig. 2b, the ability for an LCE to hold its programmed curvature is strongly influenced by the ratio of the Young's moduli after the first and second curing steps. The normalized curvature increases with the modulus ratio, indicating that a progressively stronger second network is better able to hold the curled shape. This supports the picture of a competitive double network structure and provides a simple metric for determining whether a particular composition will lead to LCEs that can retain a programmed shape.

The dependence of κ_n on the excess acrylate and PETMP contents is shown in Fig. 2c and demonstrates that LCEs are able to retain the programmed shape only for sufficiently high excess acrylate contents. κ_n increases from 0 to 1 with increasing excess acrylate content for all LCEs. Increasing the PETMP content, which results in a higher crosslink density of the first network, generally results in a decrease in κ_n. This demonstrates that too high of a crosslink density in the first network or too low of a crosslink density in the second network is detrimental to shape programming. At a very low PETMP thiol content of 10%, programming a curled shape is also unsuccessful, which we attribute to the poor mechanical properties of the first network and weak coupling between the network and nematic director during shape programming.

The data shown in Fig. 2d demonstrate that LCEs can return to a flat sheet on heating ($f < 0.125$ mm) only below a threshold excess acrylate content. At too high of an excess acrylate content, the second network dominates and the LCE retains a curled shape at temperatures above the T_{NI}. Furthermore, increasing the PETMP content results in an increased crosslink density of the first network and a smaller value of f, indicating a flatter LCE sheet at elevated temperatures.

Altogether, these studies demonstrate that a balanced composition and crosslink densities of the first and second networks are needed to achieve the programmed curvature and return to a flat LCE sheet on heating. κ_n values near 1 are associated with relatively strong second networks and larger excess acrylate contents, while low f values are associated with a relatively strong first network, which corresponds to lower excess acrylate and higher PETMP contents. The optimal composition range for an LCE that can both hold its mechanically programmed curvature ($\kappa_n \approx 1$) and return to its initial shape ($f < 0.125$ mm) is indicated in the shaded regions of Fig. 2c and d. The samples that fall in the optimal range for both $\kappa_n \approx 1$ and $f \approx 0$ contain approximately 25% PETMP content and 10% excess acrylate. This composition of LCE is used in shape programming studies described below.

While a correct balance between the first and second networks is necessary to enable shape programming, it is also critical that the deformation re-orients the liquid crystal director in order to program a desired shape. Prior studies with LCEs have shown that mesogens align parallel to tensile forces and perpendicular to compressive forces.[26,67] Therefore, curling an LCE results in parallel alignment of the nematic director along

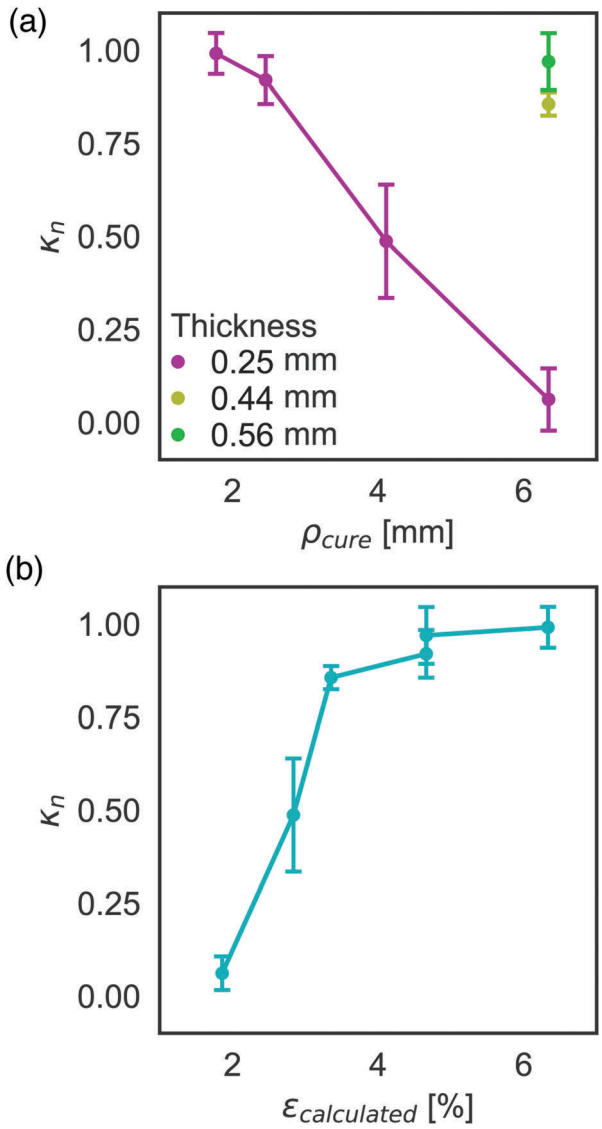

Fig. 3 (a) Normalized curvature as a function of radius of curvature, ρ_{cure}, and sample thicknesses, t, and (b) as a function of calculated maximum strain, $\varepsilon_{calculated} = t/(2\rho_{cure})$, in the LCE. ($n = 5$, error bars indicate 95% confidence intervals of the mean) numerical data is listed in Table S3 (ESI†).

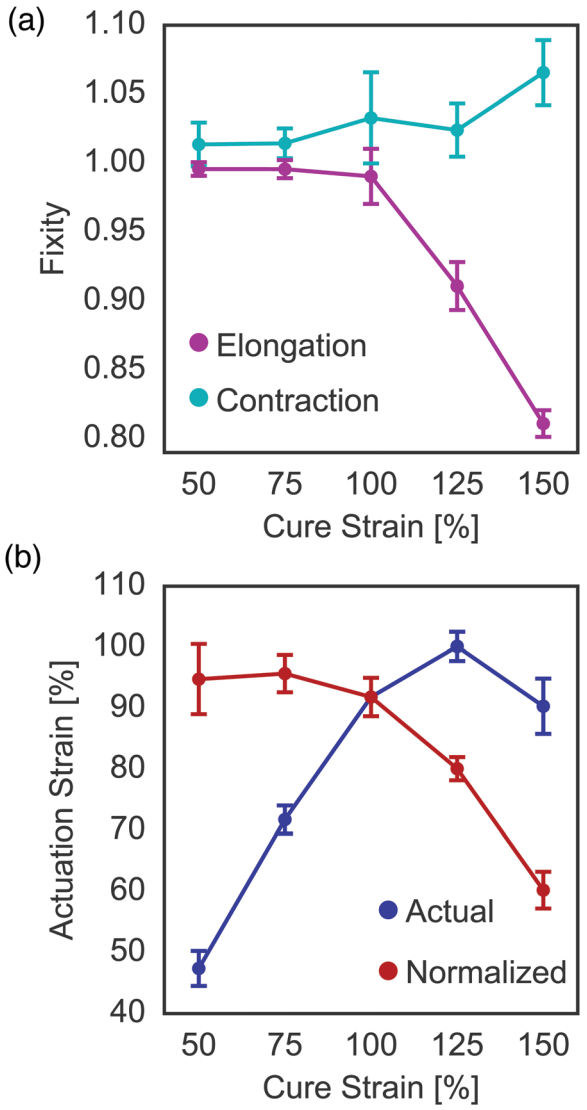

Fig. 4 (a) Elongation and contraction fixity, and (b) actual and normalized actuation strain as a function of cure strain. ($n = 5$, error bars indicate 95% confidence intervals of the mean) numerical data is reported in Table S4 (ESI†).

the outer edge and oblate perpendicular alignment along the inner edge due to tension and compression, respectively. This is demonstrated in schematically in Fig. 1a and in the cross-polarized micrographs in Fig. S3 (ESI†) which show a curled LCE imaged through its thickness. For a perfectly uniaxially aligned LCE the cross-polarized images would show a dark image when the polarizes are parallel and perpendicular to the director. As the polarizers are rotated the image would brighten to a peak intensity when the polarizes are angled 45 relative to the director. An unaligned LCE would show no intensity difference between the two images. The intensity difference between the micrographs in Fig. S3 (ESI†) occur along the inner and outer edge suggesting that there is partial alignment of the liquid crystal director along those edges. Only partial alignment is expected due to the low strain applied during deformation.

We sought to determine the minimum strain that could be used to successfully re-orient and shape-program the LCE. For a curling deformation, the largest strains occur on the outer and inner edges of the sample, which experience tension and compression, respectively. The maximum strain ε_{max} increases linearly with thickness and inversely with radius of curvature: $\varepsilon_{max} = t/(2\rho)$, where t is the LCE thickness and ρ is the radius of curvature assuming a neutral axis of bending at $t/2$. To determine the minimum necessary strain, we measured κ_n as a function of both the sample thickness t and curling radius ρ. As shown in Fig. 3, κ_n decreases with larger ρ and with decreasing t, as expected due to decreasing sample strain. Plotting κ_n against the calculated maximum strains in Fig. 3b, we find that a strain of roughly 4% is sufficient to program a desired curved shape; κ_n is greater than 0.9 for strains of 4% or higher.

We also determined the maximum strain that could be mechanically shape-programmed in LCEs using uniaxial extension. After the first crosslinking reaction, LCE samples were uniaxially stretched and UV-cured at varying linear strains. The elongational and contraction fixities were quantified as described in the Experimental section. The elongational and contraction fixities reflect the amount of strain that can be programmed in an LCE and the amount of residual strain that remains relative to the initial length on heating the LCE above the T_{NI}, respectively. Fig. 4a shows that both the elongation and contraction fixities remain near the ideal value of 1 up to a cure strain of 100%. Above 100% cure strain the contraction fixity increases, reflecting an increasing residual strain in the sample above the T_{NI}. The elongational fixity also decreases, which shows that the LCE does not fully lock-in the elongation applied during shape programming. The actuation strains of the samples are shown in Fig. 4b showing a strong decrease in the normalized actuation strains for cure strains greater than 100%. The actuation strain peaks at a value near 100% for a cure strain of 125%.

Practically, this means that strains between 4% and 100% can be adequately programmed using our optimized LCE network, but below or above these amounts the LCE will neither fully return to its initial shape nor will maintain its programmed shape. Knowing these lower and upper strain bounds is useful for designing LCE shapes. To achieve small, tight curvatures, it will be best to use thin LCEs that do not exceed 100% strain when deformed. On the other hand, thicker LCEs are required for programming shapes with broad features and large curvatures so that the imparted strain does not fall below 4%. However, care should be taken when increasing the thickness of the LCEs to ensure complete removal of solvent from the LCE before programming and that the LCE can be adequately UV cured through the thickness.

To quantify director alignment as a function of strain applied, we obtained 2D wide-angle X-ray scattering (WAXS) measurements of LCEs that were UV cured after applying uniaxial strains ranging from 0% to 150% (see Fig. S4, ESI†). At and above 25% cure strains, WAXS patters show a clear anisotropy in the

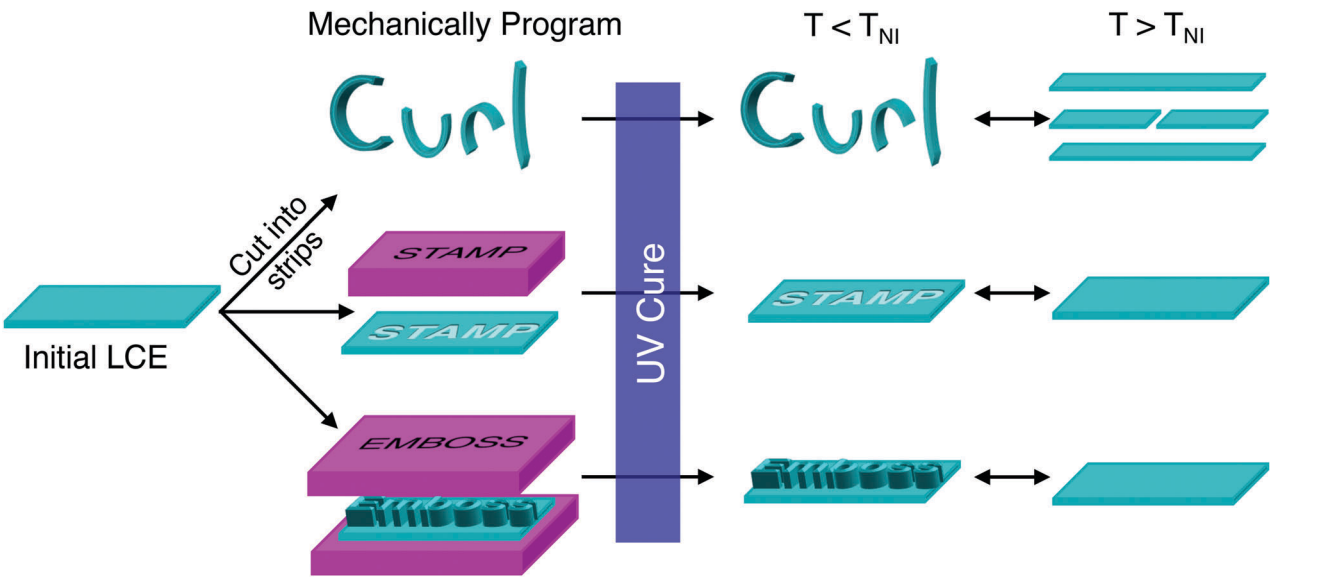

Fig. 5 Schematic detailing how LCEs are mechanically programmed *via* curling, stamping or embossing to achieve reversible shape-shifting between the initial and programmed shapes.

director orientation, reflecting a strain-induced alignment parallel to the stretching direction. The anisotropy and macroscopic order parameter increase with strain up to 100%, beyond which the order parameter plateaus at a maximum value of 0.66. At lower strains (5–15%) a clear anisotropy is not evident in the 2-D WAXS patterns. This reflects weak alignment of the nematic director. The nematic director is only weakly ordered at these strains. LCEs shape programmed over this low strain range still appear hazy due to the low degree of director alignment. Plotting the diffracted intensity over all angles reveals some anisotropy that increases with strain (see Fig. S4, ESI†). As shown in Fig. 3b, this weak anisotropy is sufficient to produce very low strains associated with curling, and being able to program low-strain deformations is important for producing topographical images, as demonstrated below.

To further verify that liquid crystal ordering was necessary to achieve reversible shape programming, we also synthesized LCEs where the second crosslinking step was conducted at temperatures above the T_{NI}. Samples were curled, heated, and UV cured at temperatures above the T_{NI}. The resulting LCEs exhibited some residual curling in the isotropic phase but with less curvature than that applied during curing. When cooled, the sample transitioned to the nematic phase and the LCE unpredictably morphed into a pretzel shape as shown in Fig. S5 (ESI†). It is unclear what drives this shape change to the pretzel configurations, but this demonstrates that liquid crystal ordering plays an important role in shape programming and is necessary for mechanical programming of reversible shape changes in LCEs.

Applying the optimized double network chemistry and knowledge of the threshold strain for shape programming

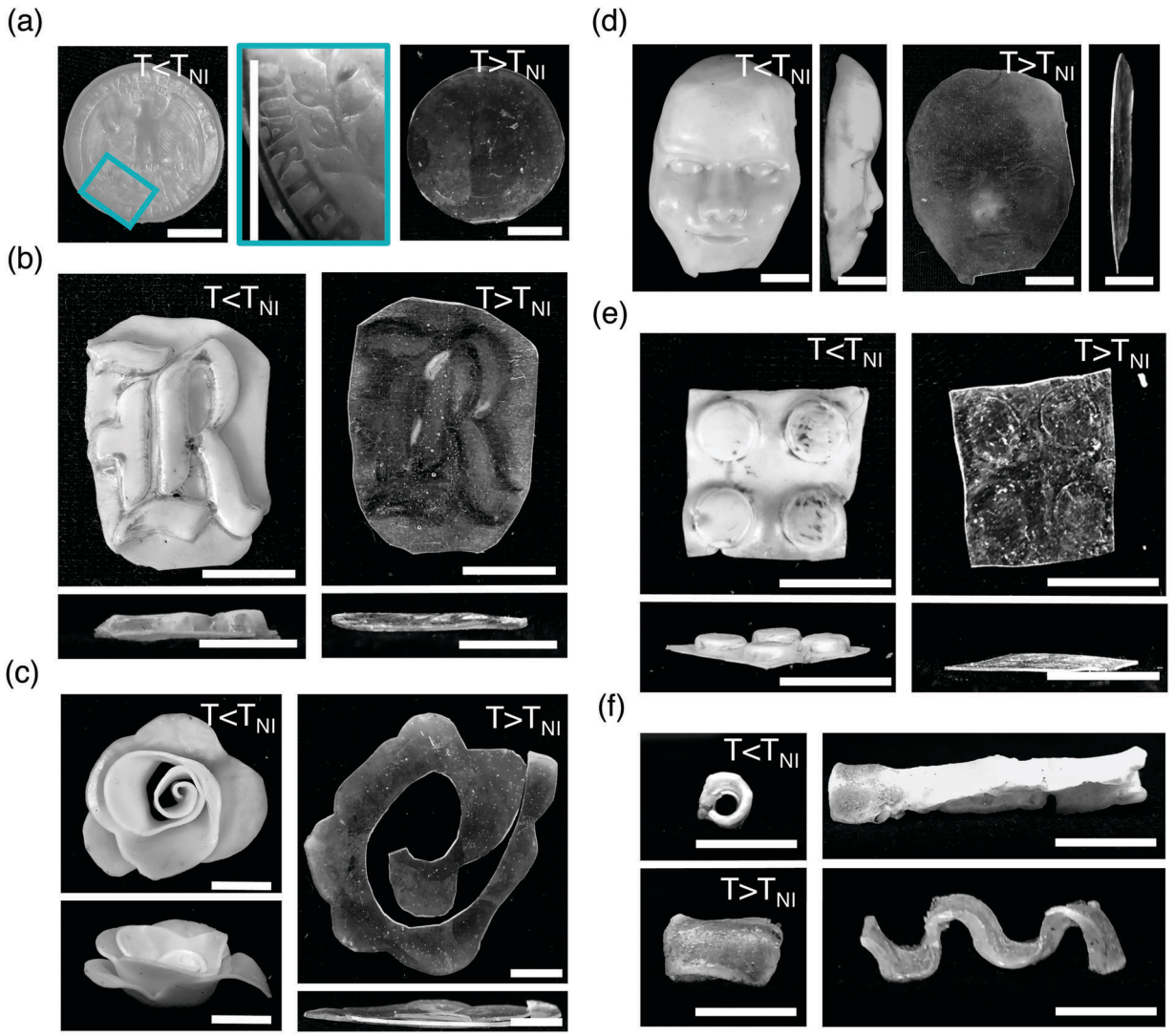

Fig. 6 Photographs of shape-programmed LCEs at $T < T_{NI}$ and $T > T_{NI}$. (Scale bars = 10 mm) (a) Initially flat LCE (t = 0.25 mm) stamped with a quarter and cured, with an enlarged region shown in blue (Mirror images are shown). (b) Initially flat LCE (t = 0.25 mm) embossed with a Rice University logo, and cured. (c) Initially flat LCE (t = 0.45 mm) that was cut, hand curled into a flower, and cured. (d) Initially flat LCE (t = 0.45 mm) pressed into a silicone mold of a face and cured. (e) Initially flat LCE (t = 0.25 mm) embossed with a Lego®, and cured. (f) LCE wave (t = 1 mm) that was flattened, curled around a rod and cured.

enabled us to program a variety of complex shapes through curling, stamping, and embossing as demonstrated in Fig. 5. This general technique of mechanically programming complex, non-planar shapes can be extended to virtually any shape or texture, including LCEs that are not initially flat. A variety of molds and textures used to program shape changes in LCE are shown in the Fig. S1 (ESI†).

First, a topographical replication of a quarter was produced. (250 μm thick, Fig. 6a) When the LCE is heated above T_{NI} it returns to a its initial smooth surface, and upon cooling the topographical features re-appear.

The embossed Rice University logo and Lego® LCEs (250 μm thick) can fully transition between their initial and programmed shapes. While some residual liquid crystal alignment can be observed, the topography disappears above T_{NI}. (Fig. 6b, e and Videos S1, S2, ESI†)

The flower LCE could reversibly curl from a flat film into a flower (450 μm thick, Fig. 6c and Video S3, ESI†).

A topographical map of a face is capable of reversibly shifting between a flat film and 3D face (450 μm thick, Fig. 6d and Video S4, ESI†). A thicker LCE (0.45 mm) was required to reproduce the face to capture the broad features of the face such as the forehead and cheeks which are associated with very low strains. For thinner LCEs, the strains associated with these features are insufficient to align and shape-program the LCE. A comparison of imprinting the face into thin and thick LCE samples is presented in the Fig. S6 (ESI†) to demonstrate this comparison.

Finally, to demonstrate the capability to program reversible shape changes between two non-planar shapes, an LCE retained the initially cured wave shape for elevated temperatures, and for temperatures below T_{NI} assumed an elongated, curled conformation. (1 mm thick, Fig. 6f and Video S5, ESI†)

These examples illustrate the ease and versatility of directly programming LCE shape changes using various mechanical deformation techniques. Other examples include an LCE that transitions between a sheet with bumps and a flat sheet (Fig. S2b and Video S6, ESI†), and an LCE that transitions between textured flat LCE sheet and an LCE with a series of steps (Fig. S2a and Video S7, ESI†) Further details and additional images of programmed LCEs are included in the ESI.†

4. Conclusion

In summary, we demonstrate the ability to directly program complex reversible curvatures into LCEs using mechanical deformations. By carefully optimizing the LCE network composition, a variety of complex shapes can be programmed through curling, stamping, stretching, and embossing, and the method is not limited to initially flat LCEs. This work demonstrates that concepts that have been developed for isotropic double network elastomers are applicable and useful for optimization of shape changes in LCEs. This work also widens the potential application of LCEs in biomedical devices, soft-robotics and micro-fluidics where arbitrary and easily programmed shapes are needed. Future work using this method includes imprinting microchannels for micro-fluidic devices, topological pixels for braille displays or dynamic buttons, and 3D printing complex structures where the print path is not constrained to desired alignment profiles.

Conflicts of interest

The authors declare no competing financial interests.

Acknowledgements

The authors acknowledge support from the Welch Foundation for Chemical Research (C-1888), the Army Research Office Chemical Sciences Division (W911NF1810289), and the Shared Equipment Authority at Rice University.

References

1 T. J. White and D. J. Broer, *Nat. Mater.*, 2015, **14**, 1087–1098.
2 M. Wang, S. M. Sayed, L. X. Guo, B. P. Lin, X. Q. Zhang, Y. Sun and H. Yang, *Macromolecules*, 2016, **49**, 663–671.
3 Y. Yang, W. Zhan, R. Peng, C. He, X. Pang, D. Shi, T. Jiang and Z. Lin, *Adv. Mater.*, 2015, **27**, 6376–6381.
4 C. Yuan, D. J. Roach, C. K. Dunn, Q. Mu, X. Kuang, C. M. Yakacki, T. J. Wang, K. Yu and H. J. Qi, *Soft Matter*, 2017, **13**, 5558–5568.
5 W. Liu, L. X. Guo, B. P. Lin, X. Q. Zhang, Y. Sun and H. Yang, *Macromolecules*, 2016, **49**, 4023–4030.
6 H. Zeng, P. Wasylczyk, D. S. Wiersma and A. Priimagi, *Adv. Mater.*, 2018, **30**, 1–9.
7 T. Okamoto, K. Urayama and T. Takigawa, *Soft Matter*, 2011, **7**, 10585–10589.
8 S. K. Ahn, T. H. Ware, K. M. Lee, V. P. Tondiglia and T. J. White, *Adv. Funct. Mater.*, 2016, **26**, 5819–5826.
9 H. Jiang, C. Li and X. Huang, *Nanoscale*, 2013, **5**, 5225.
10 A. Agrawal, H. Chen, H. Kim, B. Zhu, O. Adetiba, A. Miranda, A. Cristian Chipara, P. M. Ajayan, J. G. Jacot and R. Verduzco, *ACS Macro Lett.*, 2016, **5**, 1386–1390.
11 V. Gimenez-Pinto, F. Ye, B. Mbanga, J. V. Selinger and R. L. Selinger, *Sci. Rep.*, 2017, **7**, 1–7.
12 H. Zeng, O. M. Wani, P. Wasylczyk, R. Kaczmarek and A. Priimagi, *Adv. Mater.*, 2017, **29**, 1–7.
13 C. Wang, K. Sim, J. Chen, H. Kim, Z. Rao, Y. Li, W. Chen, J. Song, R. Verduzco and C. Yu, *Adv. Mater.*, 2018, **30**, 43–71.
14 Y. Gao, T. Mori, S. Manning, Y. Zhao, A. D. Nielsen, A. Neshat, A. Sharma, C. J. Mahnen, H. R. Everson, S. Crotty, R. J. Clements, C. Malcuit and E. Hegmann, *ACS Macro Lett.*, 2016, **5**, 4–9.
15 K. Urayama, *Macromolecules*, 2007, **40**, 2277–2288.
16 C. Ohm, M. Brehmer and R. Zentel, *Adv. Mater.*, 2010, **22**, 3366–3387.
17 A. Konya, V. Gimenez-Pinto and R. L. B. Selinger, *Front. Mater.*, 2016, **3**, 1–7.
18 D. Martella and C. Parmeggiani, *Chem. – Eur. J.*, 2018, **24**, 12206–12220.
19 M. E. Prévôt, S. Ustunel and E. Hegmann, *Materials*, 2018, **11**, 377.

20 M. Yamada, M. Kondo, J. I. Mamiya, Y. Yu, M. Kinoshita, C. J. Barrett and T. Ikeda, *Angew. Chem., Int. Ed.*, 2008, **47**, 4986–4988.
21 O. M. Wani, H. Zeng and A. Priimagi, *Nat. Commun.*, 2017, **8**, 1–7.
22 H. Zeng, O. M. Wani, P. Wasylczyk and A. Priimagi, *Macromol. Rapid Commun.*, 2018, **39**, 1–6.
23 A. H. Gelebart, D. Jan Mulder, M. Varga, A. Konya, G. Vantomme, E. W. Meijer, R. L. Selinger and D. J. Broer, *Nature*, 2017, **546**, 632–636.
24 H. Tian, Z. Wang, Y. Chen, J. Shao, T. Gao and S. Cai, *ACS Appl. Mater. Interfaces*, 2018, **10**, 8307–8316.
25 H. Shahsavan, S. M. Salili, A. Jákli and B. Zhao, *Adv. Mater.*, 2015, **27**, 6828–6833.
26 J. Küpfer and H. Finkelmann, *Die Makromol. Chemie, Rapid Commun.*, 1991, **12**, 717–726.
27 Z. Pei, Y. Yang, Q. Chen, E. M. Terentjev, Y. Wei and Y. Ji, *Nat. Mater.*, 2014, **13**, 36–41.
28 C. M. Yakacki, M. Saed, D. P. Nair, T. Gong, S. M. Reed and C. N. Bowman, *RSC Adv.*, 2015, **5**, 18997–19001.
29 M. Warner and E. M. Terentjev, *Liquid Crystal Elastomers*, Oxford University Press, Oxford, England, 2003.
30 A. Agrawal, P. Luchette, P. Palffy-Muhoray, S. L. Biswal, W. G. Chapman and R. Verduzco, *Soft Matter*, 2012, **8**, 7138.
31 F. Greco, V. Domenici, A. Desii, E. Sinibaldi, B. Zupančic, B. Zalar, B. Mazzolai and V. Mattoli, *Soft Matter*, 2013, **9**, 11405.
32 R. R. Kohlmeyer and J. Chen, *Angew. Chem., Int. Ed.*, 2013, **52**, 9234–9237.
33 J. M. Boothby and T. H. Ware, *Soft Matter*, 2017, **13**, 4349–4356.
34 J. J. Wie, K. M. Lee, T. H. Ware and T. J. White, *Macromolecules*, 2015, **48**, 1087–1092.
35 H. Zeng, D. Martella, P. Wasylczyk, G. Cerretti, J. C. G. Lavocat, C. H. Ho, C. Parmeggiani and D. S. Wiersma, *Adv. Mater.*, 2014, **26**, 2319–2322.
36 G. Babakhanova, T. Turiv, Y. Guo, M. Hendrikx, Q. H. Wei, A. P. Schenning, D. J. Broer and O. D. Lavrentovich, *Nat. Commun.*, 2018, **9**, 1–9.
37 S. J. Abhoff, F. Lancia, S. Iamsaard, B. Matt, T. Kudernac, S. P. Fletcher and N. Katsonis, *Angew. Chem., Int. Ed.*, 2017, **56**, 3261–3265.
38 S. Iamsaard, S. J. Aßhoff, B. Matt, T. Kudernac, J. J. Cornelissen, S. P. Fletcher and N. Katsonis, *Nat. Chem.*, 2014, **6**, 229–235.
39 H. Shahsavan, S. M. Salili, A. Jakli and B. Zhao, *Adv. Mater.*, 2017, **29**, 1–7.
40 P. Plucinsky, M. Lemm and K. Bhattacharya, *Phys. Rev. E*, 2016, **94**, 1–5.
41 H. Aharoni, Y. Xia, X. Zhang, R. D. Kamien and S. Yang, *Proc. Natl. Acad. Sci. U. S. A.*, 2018, **115**, 7206–7211.
42 T. H. Ware, M. E. McConney, J. J. Wie, V. P. Tondiglia and T. J. White, *Science*, 2015, **347**, 982–984.
43 M. E. McConney, A. Martinez, V. P. Tondiglia, K. M. Lee, D. Langley, I. I. Smalyukh and T. J. White, *Adv. Mater.*, 2013, **25**, 5880–5885.
44 A. Kotikian, R. L. Truby, J. W. Boley, T. J. White and J. A. Lewis, *Adv. Mater.*, 2018, **30**, 1–6.
45 C. P. Ambulo, J. J. Burroughs, J. M. Boothby, H. Kim, M. R. Shankar and T. H. Ware, *ACS Appl. Mater. Interfaces*, 2017, **9**, 37332–37339.
46 H. Aharoni, E. Sharon and R. Kupferman, *Phys. Rev. Lett.*, 2014, **113**, 1–5.
47 B. A. Kowalski, C. Mostajeran, N. P. Godman, M. Warner and T. J. White, *Phys. Rev. E*, 2018, **97**, 1–5.
48 Z. L. Wu, M. Moshe, J. Greener, H. Therien-Aubin, Z. Nie, E. Sharon and E. Kumacheva, *Nat. Commun.*, 2013, **4**, 1586–1587.
49 C. Ahn, X. Liang and S. Cai, *Extrem. Mech. Lett.*, 2015, **5**, 30–36.
50 L. Yu, H. Shahsavan, G. Rivers, C. Zhang, P. Si and B. Zhao, *Adv. Funct. Mater.*, 2018, **28**, 1802809.
51 R. D. Andrews, A. V. Tobolsky and E. E. Hanson, *J. Appl. Phys.*, 1946, **17**, 352–361.
52 L. G. Baxandall and S. F. Edwards, *Macromolecules*, 1988, **21**, 1763–1772.
53 A. S. Aprem, K. Joseph and S. Thomas, *J. Appl. Polym. Sci.*, 2004, **91**, 1068–1076.
54 S. Kaang, D. Gong and C. Nah, *J. Appl. Polym. Sci.*, 1997, **65**, 917–924.
55 P. J. Flory, *Trans. Faraday Soc.*, 1960, **56**, 722–743.
56 N. K. Singh and A. J. Lesser, *Macromolecules*, 2011, **44**, 1480–1490.
57 D. R. Rottach, J. G. Curro, G. S. Grest and A. P. Thompson, *Macromolecules*, 2004, **37**, 5468–5473.
58 Y. Meng, J. Jiang and M. Anthamatten, *ACS Macro Lett.*, 2015, **4**, 115–118.
59 J. Zhou and S. S. Sheiko, *J. Polym. Sci., Part B: Polym. Phys.*, 2016, **54**, 1365–1380.
60 A. Lendlein, H. Jiang, O. Junger and R. Langer, *Nature*, 2005, **434**, 879–882.
61 Q. Zhao, H. J. Qi and T. Xie, *Prog. Polym. Sci.*, 2015, **49-50**, 79–120.
62 S. Schauer, T. Meier, M. Reinhard, M. Röhrig, M. Schneider, M. Heilig, A. Kolew, M. Worgull and H. Hölscher, *ACS Appl. Mater. Interfaces*, 2016, **8**, 9423–9430.
63 T. Meier, J. Bur, M. Reinhard, M. Schneider, A. Kolew, M. Worgull and H. Hölscher, *J. Micromech. Microeng.*, 2015, **25**, 065017.
64 M. Deutsch, *Phys. Rev. A: At., Mol., Opt. Phys.*, 1991, **44**, 8264–8270.
65 P. Davidson, D. Petermann and A. M. Levelut, *J. Phys. II*, 1995, **5**, 113–131.
66 M. O. Saed, A. H. Torbati, C. A. Starr, R. Visvanathan, N. A. Clark and C. M. Yakacki, *J. Polym. Sci., Part B: Polym. Phys.*, 2017, **55**, 157–168.
67 A. Agrawal, A. C. Chipara, Y. Shamoo, P. K. Patra, B. J. Carey, P. M. Ajayan, W. G. Chapman and R. Verduzco, *Nat. Commun.*, 2013, **4**, 1739.

ACS APPLIED MATERIALS & INTERFACES

www.acsami.org

Research Article

Reactive 3D Printing of Shape-Programmable Liquid Crystal Elastomer Actuators

Morgan Barnes, Seyed M. Sajadi, Shaan Parekh, Muhammad M. Rahman,* Pulickel M. Ajayan,* and Rafael Verduzco*

Cite This: *ACS Appl. Mater. Interfaces* 2020, 12, 28692–28699

Read Online

ACCESS | Metrics & More | Article Recommendations | Supporting Information

ABSTRACT: 3D printed, stimuli-responsive materials that reversibly actuate between programmed shapes are promising for applications ranging from biomedical implants to soft robotics. However, current 3D printing of reversible actuators significantly limits the range of possible shapes and/or shape responses because they couple the print path to mathematically determined director profiles to elicit a desired shape change. Here, we report a reactive 3D-printing method that decouples printing and shape-programming steps, enabling a broad range of complex architectures and virtually any arbitrary shape changes. This method involves first printing liquid crystal elastomer (LCE) precursor solution into a catalyst bath, producing complex architectures defined by printing. Shape changes are then programmed through mechanical deformation and UV irradiation. Upon heating and cooling, the LCE reversibly shape-shifts between printed and programmed shapes, respectively. The potential of this method was demonstrated by programming a variety of arbitrary shape changes in a single printed material, producing auxetic LCE structures and symmetry-breaking shape changes in LCE sheets.

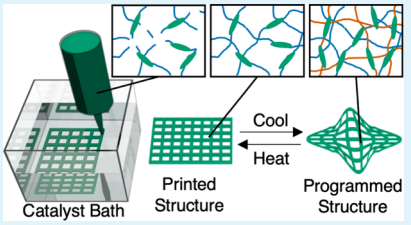

KEYWORDS: *3D printing, soft actuators, liquid crystal elastomers, shape morphing, smart materials*

INTRODUCTION

3D printing has made widespread impact across science, engineering, and industry by producing materials with complex architectures that would be difficult or impossible to create using conventional fabrication methods.[1−7] For some applications, including soft-robotics or biomedical devices, there is interest in active materials that can respond to external stimuli by undergoing reversible shape changes.[8,9] These can be achieved through 4D printing, which combines 3D printing with active materials to produce stimuli-responsive materials with complex architectures that can change shape over a fourth dimension (e.g., time or temperature). For example, 4D printed hydrogels change shape with water content and temperature and have been used to fabricate biomimetic flower-like structures.[10] 4D printed shape-memory elastomers have been used to produce stents or soft grippers that expand when heated.[11] Also, 4D printed liquid crystal elastomers (LCEs) show fully reversible shape changes and have been implemented in the development of soft, temperature-responsive actuators.[2,3,12,13]

Four-dimensional printing is inherently more complex than 3D printing because it requires simultaneously printing a structure and defining or programming a shape response in the resulting material. One strategy for shape programming involves fabricating multilayered structures which vary spatially in cross-link density, resulting in curling, buckling, or twisting with changes in temperature or degree of swelling.[14−16] An alternative method to produce more complex shape changes uses shear forces during printing to align the material.[3,10,15] The printed fibers then undergo anisotropic network conformational changes in response to changes in temperature or because of swelling.[17−19] Using these methods, complex shape changes can be achieved by printing along predefined paths that elicit localized out-of-plane bending. However, this couples the shape change to the print path and restricts 4D printed layers to in-plane alignment rather than alignment in both the in- and out-of-plane directions. Further, achieving a desired shape response requires solving the inverse mathematical problem that relates the shape change to the local alignment of the material. These approaches therefore significantly limit the shape and/or shape response that can be produced.

Here, we present a versatile 3D printing method that decouples the printing and shape programming steps to provide access to a broad range of architectures and virtually arbitrary shape changes. We printed LCEs because they are particularly promising materials for soft robotics and actuators where untethered actuation in response to thermo-, photo-, or electrostimuli is desired.[20−25] LCEs are cross-linked polymer

Received: April 21, 2020
Accepted: June 2, 2020
Published: June 2, 2020

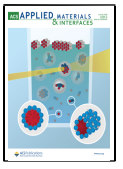

https://dx.doi.org/10.1021/acsami.0c07331
ACS Appl. Mater. Interfaces 2020, 12, 28692−28699

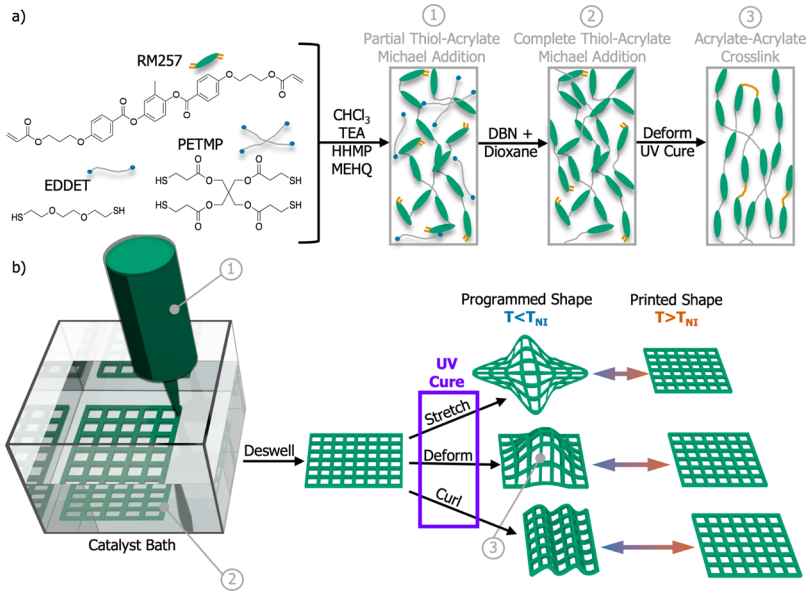

Figure 1. Schematic of reactive 4D printing and shape programming of LCEs. (a) LCE synthetic scheme showing the network-forming components and three distinct reactive steps during the fabrication process. (b) Schematic for the 4D printing of LCEs involving printing in a catalyst bath followed by deforming and UV curing for shape programming. The resulting LCE exhibited reversible shape changes between the printed and programmed structures when heated and cooled, respectively.

networks with a low glass transition temperature and liquid crystal ordering. In nematic LCEs, the polymer conformation is coupled to the orientation of the liquid crystal director, and as a result, changes to the order parameter can produce bulk shape changes in the material. Shape changes can be programmed into an LCE by dictating a specific nematic director orientation, for example, through patterned surfaces or mechanical deformation.[26−30] Recent work demonstrated the preparation of LCEs through 3D printing and successfully achieved a variety of complex shape and programmed shape changes.[31] However, these studies relied on shear alignment to define the local nematic director, which couples the alignment to the print path. In this study, we decoupled the printing and shape-programming steps to achieve virtually arbitrary shape changes in 3D printed LCEs.

The reactive 3D printing approach is shown schematically in Figure 1 and, briefly, involves reactive printing an LCE network into a catalyst bath followed by drying and mechanical shape programming. The process uses orthogonal base- and UV-activated reactions. When heated above or cooling below the nematic-to-isotropic transition temperature ($T_{NI} \approx 75$ °C, Figure S1, Supporting Information), the resulting LCE can shape-shift between the initial shape defined by printing and the mechanically deformed shape, respectively. This method does not require designating a specific print path or defining a specific liquid crystal director orientation during printing and is not limited to shape changes with currently known director fields and specified print paths. This enables the fabrication of a variety of shape-shifting LCEs that would be difficult or impossible to print using traditional printing methods and could be useful for the wider 3D-printing community.

EXPERIMENTAL SECTION

Materials. 2,2′-(Ethylenedioxy)diethanethiol (EDDET), pentaerythritol tetrakis (3-mercaptopropionate) (PETMP), 1,4-bis-[4-(3-acryloyloxypropyloxy)benzoyloxy]-2-methylbenzene (RM257), chloroform, triethyl amine (TEA), 1,5-diazabicyclo[4.3.0]non-5-ene (DBN), chloroform ($CHCl_3$), 1,4 dioxane, 4-methoxyphenol (MEHQ), and (2-hydroxyethoxy)-2-methylpropiophenone (HHMP) were obtained from commercial suppliers and used as received.

LCE Synthesis. The following procedure is for an LCE with 10 mol % excess acrylate and 25 mol % of the thiols coming from PETMP. First, RM257 (4000 mg), 1 wt % HHMP (40 mg), and 0.25 wt % MEHQ (10 mg) were dissolved in chloroform (3 mL) at 70 °C. MEHQ is an inhibitor that minimizes radical-induced acrylate crosslinking during processing and printing, and the HHMP served as the radical photoinitiator for the final UV-induced mechanical programming step. After the mixture cooled to room temperature, 83% of EDDET (700.12 mg) and PETMP (312.87 mg) were added followed by 20 μL of TEA. The mixture was vortexed to ensure proper mixing and then cured overnight at 70 °C. Next day, the viscous solution was diluted by adding 5 mL of chloroform and the remaining EDDET (144 mg) and PETMP (64.37 mg). Next, the mixture was inserted into the 3D printer syringe and printed into a Petri dish filled with a 2 μL/mL DBN in the dioxane catalyst bath. At this stage, the sample was soft but could be carefully removed from the solvent bath, and the sample was dried by heating to 80 °C overnight remove chloroform and dioxane. Finally, the LCE was mechanically deformed to the desired shape and irradiated with 365 nm light for 10 min to complete the second cure step. Bulk synthesized LCEs were synthesized using previously reported procedures.[31]

3D Printing. 3D printing was performed on a Hyrel 3D printer (model: Engine HR) at room temperature with a 20- or 22-gauge syringe blunt needle and a speed of 10 mm/s into a 2 vol % DBN in dioxane solution in a glass Petri dish.

Normalized Curvature and Actuation. Normalized curvature was calculated following the same procedure as previously reported.[31] LCE strips were wrapped around rods of known radii and UV-cured. The resulting LCE was heated ($T \approx 120$ °C) and cooled ($T \approx$ room temperature) once to remove any residual stresses. The LCE was photographed, and image analysis was used to extract the radius of the curvature. Normalized actuation was calculated as $\rho_{LCE}/(\rho_{rod} + t/2)$, where ρ_{LCE} is the radius of curvature of the LCE, ρ_{rod} is the radius of curvature of the rod the LCE was curled around, and t is the LCE thickness. Normalized actuation was determined by stretching LCE to 50, 75, 100, and 125% strains and UV curing. After heating and cooling the LCE once to remove residual stresses, the length of the

https://dx.doi.org/10.1021/acsami.0c07331
ACS Appl. Mater. Interfaces 2020, 12, 28692−28699

LCE at room temperature and above the T_{NI} was recorded. Actuation strain was calculated as the change in length of the LCE divided by the heated contracted length. Normalized actuation was calculated as the ratio of the actual actuation of the LCE to the programmed strain.

Mechanical Testing. A TA Instruments Ares G2 was used for dynamic mechanical analysis. Young's modulus was obtained by stretching a rectangular LCE by a Hencky strain rate of 5%/min. A linear fit was applied to the stress versus strain curve from 0 to 1.5% strain with the slope of the line being Young's modulus. Stress versus strain curves until failure were obtained by loading the rectangular LCE strip cut either parallel or perpendicular to the printing path into a linear rectangular clamp. The sample was then stretched at a linear strain rate of 200% per minute until failure.

Swelling. Swelling tests were performed by submerging a bulk-synthesized LCE before UV curing into various solvents for 24 h. The weight of the LCEs before and after swelling was recorded, and the swelling was calculated as the mass gained from swelling divided by the initial mass of the dry LCE.

Rheology. A TA Instruments Ares G2 was used for all rheology data with a 25 mm 0.1 rad cone and plate geometry. Data were collected immediately after adding the remaining solvent and thiol monomers to the reacted oligomer solution. Storage and loss moduli as a function of time were obtained under oscillation with a strain of 3% and a frequency of 1 Hz for 5 h. The viscosity was determined under steady shear, with the shear rate varying from 0.001 to 1000 1/s.

Differential Scanning Calorimetry. TA Instruments Q20 was used to obtain differential scanning calorimetry curves. Samples were equilibrated at −20 °C and ramped to 100 °C at 5 °C/min. The sample was held at 100 °C for 5 min and ramped down to −20 °C at 5 °C/min and held at that temperature for 5 min. The cycle was repeated, and T_g and T_{NI} were obtained from the second heating cycle from the inflection point and local minimum, respectively.

RESULTS AND DISCUSSION

LCEs are double-network elastomers commonly fabricated using "two-step" cross-linking chemistries. Generally, these involve an initial cross-linking reaction to produce a lightly cross-linked elastomer followed by mechanical elongation and further crosslinking.[32] At room temperature, the LCE will assume the elongated shape, but when heated, it will return to the contracted shape of the lightly cross-linked elastomer. A number of different chemistries have been implemented in the synthesis of LCEs, in particular, a widely used thiol−ene chemistry first reported by Yakacki et al.,[33] in which thiol−acrylate Michael addition chemistry was used to form the first network and residual acrylate functional groups are cross-linked under UV light to form the second network. Furthermore, balancing the cross-link densities of the first and second networks is important for achieving complex shape reversibility in LCEs. By doing so, simply deforming the LCE after the first cross-linking step by stretching, twisting, or embossing prior followed by UV curing can be used to create an LCE that reversibly shifts between the original shape and the deformed shape upon heating and cooling, respectively.[31]

We modified this general approach to enable 3D printing of LCEs. The reactive printing process involved sequential coupling and polymerization reactions in three steps. In the first step, the network-forming reagents RM257, EDDET, and PETMP were partially cross-linked to produce a printable oligomeric solution. In the second step, this oligomer solution was printed into a catalyst bath at room temperature, producing cross-linked LCE fibers via rapid thiol−acrylate coupling reactions during printing. Next, the sample was removed from the catalyst bath and dried to recover a polydomain nematic LCE with residual unreacted acrylate functional groups. In the third reactive step, the sample was shape-programmed by mechanical deformation and UV-cured to cross-link residual acrylate groups. The resulting shape-programmed LCE was able to switch between the printed and programmed shapes when heated and cooled, respectively.

The three-step printing process was tailored to satisfy several constraints in terms of materials processing, network composition, and solvent composition. The oligomer solution was designed such that it remained solution-processible and reacted quickly during printing to form a cross-linked fiber that maintained its shape with minimal spreading. The solvents used for printing and in the catalyst bath were chosen such that the material did not precipitate out or swell excessively during printing. Excessive swelling can produce unwanted internal stresses and curvatures in the final material. Finally, the overall network composition was chosen to enable shape programming of the final material by mechanical deformation followed by UV-induced crosslinking of excess acrylates. Specifically, we maintained a molar ratio of thiol to acrylate functional groups of 10:11 with PETMP, contributing 25 mol % of thiols in the network to achieve an appropriate balance in network cross-link densities to enable mechanical shape programming.[31]

We targeted a composition of the oligomer solution that was near to but below the gel point, enabling rapid crosslinking in the catalyst bath during printing. The oligomer solution was prepared by dissolving a portion of the thiol-containing reagents (EDDET and PETMP) with the entirety of RM257 (Table S1, Supporting Information) along with a mild amine catalyst TEA in chloroform. The TEA slowly catalyzed thiol−acrylate Michael addition reactions between RM257 and thiol-containing reagents, and after reacting at ambient conditions overnight, a viscous acrylate-capped oligomer solution was formed. We optimized the composition of the oligomer solution by successively increasing the content of thiols (maintaining a constant molar ratio of EDDET/PETMP) until the solution was no longer printable because of gelation. The mixture gelled when 85 mol % of thiols was incorporated, while 83 mol % of thiols produced a highly viscous but printable solution. Therefore, the oligomer solution composition was set to 83 mol % of thiol. This compared favorably with predictions based on the Flory−Stockmayer equation, which predicts a critical gel point of 84 mol % thiols, assuming complete conversion of the thiols. Immediately before printing, the remaining 17 mol % of thiols were added to the oligomer solution, and the solution was diluted with chloroform. We diluted the oligomer solution with chloroform prior to printing for two reasons. First, dilution decreased the overall concentration of TEA, which slowed down gelation in the presence of added thiol-containing reagents. This allowed us to obtain an LCE oligomer solution that remained printable for hours after all the reagents are mixed (Figure S2, Supporting Information). Second, this minimized excessive swelling during printing. Swelling during printing can produce severe curling because of anisotropic internal stresses, caused by anchoring of the printed fiber to the substrate along one edge. The solvent content in the print solution was set to 70 vol %, similar to the estimated solvent content in the printed LCE fibers in the catalyst bath solvent, approximately 71 vol % based on a measured degree of swelling of 250% in dioxane.

Rapid crosslinking during printing was achieved using the tertiary amine base DBN as the catalyst. DBN rapidly promotes thiol−acrylate Michael addition reactions but will not react directly with acrylates.[34] The DBN was diluted to a

https://dx.doi.org/10.1021/acsami.0c07331
ACS Appl. Mater. Interfaces 2020, 12, 28692−28699

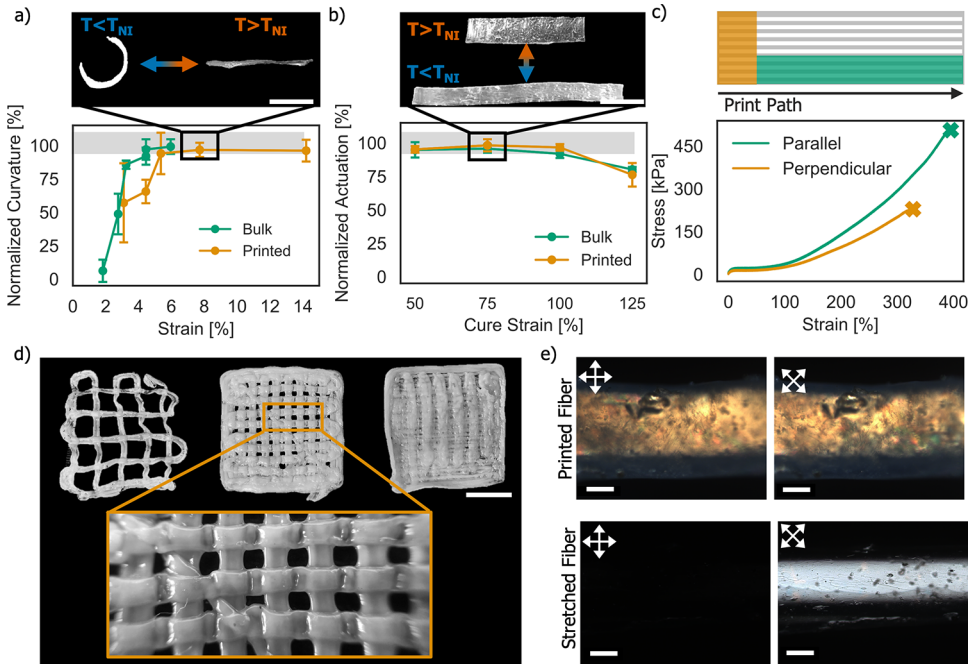

Figure 2. Photographs of printed LCE samples and analysis of LCE actuation, mechanical, and optical properties. (a,b) Normalized curvature and actuation strains of LCEs along with representative images of 4D printed samples. Normalized curvature and actuation values are used to quantify the ability to shape program samples, and the gray box indicates ideal normalized curvature and actuation windows (n = 5, error bars indicate 95% confidence intervals of the mean). (c) Stress vs strain data for a one-layer printed LCE stretched parallel and perpendicular to the print path. (d) Photograph of a two-layer LCE grid printed with decreasing distances between the fibers. Scale bar is 1 cm. (e) Cross-polarized optical micrographs of an unstretched and stretched printed fiber, showing no alignment in printed fibers until after stretching and UV crosslinking. Scale bars are 200 μm.

concentration of 2 μL/mL as higher concentrations tested (2.5 and 3 μL/mL) caused clogging of the extrusion nozzle. The oligomer solution was printed into the catalyst bath to complete the thiol−acrylate Michael addition and produce cross-linked and solvent-swollen LCE fibers.

To choose an appropriate solvent for the bath, we had to consider the solubility of the LCE, swelling of the fibers, and solvent volatility. We found that many solvents used to dilute DBN, including toluene and acetonitrile, produced LCEs with poor optical properties and that exhibited minimal actuation strains and had smaller strain-to-failure values than bulk-synthesized LCEs. These samples remained hazy in appearance even when heated above the nematic-to-isotropic transition temperature (Supporting Information, Figure S3). We observed this phenomenon in catalyst baths with solvents that were relatively poor solvents of the synthesized LCE, as reflected in the degree of swelling shown in the Supporting Information, Figure S4. However, we found that solvents with high degrees of swelling including dioxane and DMF resulted in superior LCEs. Ultimately, we chose dioxane as the catalyst bath diluent because it has a boiling point of 101 °C that is ideal for the printing process. This temperature is high enough to minimize unwanted evaporation during printing and low enough to enable complete drying of the LCE samples under vacuum overnight. Printed structures were left in the catalyst bath for at least 5 min after printing to ensure the fibers had enough time to fully swell and complete the cross-linking reaction. Upon removing and drying the LCE overnight, the structure shrank by approximately 80 vol % (a 3 cm × 3 cm printed square results in a 1.8 cm × 1.8 cm) but retained the overall shape of the printed structure with minimal curling. We did not quantify the amount of the unreacted oligomer that may have leached out into the solvent bath during printing, and further optimization may be possible by optimizing the catalyst concentration to reduce or eliminate leaching.

Ideally, printed LCE films should exhibit similar shape programmability as bulk-synthesized LCE films. We tested shape programmability by determining the lower and upper strain limits for reversible actuation using methods previously reported.[31] Briefly, the low-strain limits were obtained by curling LCEs around rods with a known radius of curvature for shape programming. We defined the normalized curvature as the ratio of the final radius of curvature of the LCE compared to the programmed curvature. The normalized curvature was 100% if we were able to perfectly program a desired shape change, and it was less than 100% if the final curvature was larger than the programmed strain. To calculate the strain associated with a given curvature, we assumed a neutral bending axis in the middle of the LCE and calculated the programmed strain $\epsilon = t/2\rho$, where t is the thickness of the LCE and ρ is the radius of curvature of the rod used in shape programming. The lower strain limit was defined as the minimum strain at which the normalized curvature was greater than 90% (denoted by the gray box in Figure 2a). To determine the upper programmable strain limit, we uniaxially stretched LCEs to 50, 75, 100, and 125% strains during shape programming. We defined the normalized actuation as the observed actuation divided by the programmed strain. Similar to the lower strain limit, the upper strain limit was defined as the maximum strain at which the normalized actuation was greater than 90% (denoted by the gray box in Figure 2b).

The programmable strain range for 3D printed LCEs (6−100%) compared favorably to that for bulk synthesized LCEs (4−100%). This large programmable strain range enables

https://dx.doi.org/10.1021/acsami.0c07331
ACS Appl. Mater. Interfaces 2020, 12, 28692−28699

LCEs to undergo complex shape changes that seamlessly merge both low strain bending (with order parameter gradients observed through the thickness of the sample) and high strain stretching deformations (with order parameter being a function of strain) into a single actuation mechanism without knowing the liquid crystal director profile, as demonstrated in prior work.[31] We also observed a reduced modulus for printed samples (Supporting Information, Figure S5). This may be because of side reactions during the reactive printing or loop defects because of network crosslinking in a highly swollen state, and we attributed the slight difference of the overall programmable strain range between bulk synthesized and printed LCEs to the reduced modulus observed for printed samples.

After determining that simple curvatures and uniaxial expansions could be programmed into printed LCE films, we analyzed the mechanical integrity of a printed LCE. We stretched rectangular strips (~15 mm × 3 mm × 0.3 mm) of a one-layer film cut both parallel and perpendicular to the print path before UV polymerization. The LCE film was stronger and had a higher strain-to-failure when stretched parallel to the fibers (in longitudinal direction) rather than perpendicular to the fibers (in transverse direction), as shown in Figure 2c. This is expected as 3D printing often results in anisotropic mechanical properties because of relatively weak adhesion between printed fibers.[35−37] Additionally, the anisotropic mechanical behavior was only observed for strain values greater than 100%, which was outside the programmable strain window (6−100% strains) for this material. Therefore, within this strain window, printed LCEs can be mechanically deformed and shape-programmed regardless of the print path. We also observed a soft elastic mechanical response when deforming the sample both in longitudinal and transverse directions to the print path. A soft elastic response is a broad plateau in the stress−strain curve and is a characteristic feature of soft liquid crystal networks that represents material deformation with little or no increase in stress.[38,39]

Next, we printed two-layer films with a weave-like architecture (90° rotation of the printed fibers between the first and second layers with increasing density of fibers), as shown in Figure 2d. We can easily control the porosity of printed films to form a grid with large, small, or no space between the printed layers. Additionally, we confirmed that no alignment was imprinted into the LCE fibers during printing using polarized optical microscopy. As shown in Figure 2e, there was no intensity difference for transmitted light when the crossed polarizers were oriented at a 0 or 45° relative to the printed fiber direction. However, after the LCE was stretched parallel to the fiber, we observed a significant intensity difference depending on the orientation of the crossed polarizers, indicating alignment of the liquid crystal director parallel to the stretching direction. Therefore, shape changes and liquid crystal alignment were only achieved through mechanical deformations of the printed structure after printing and were independent of the print path.

To demonstrate the versatility of our reactive 3D printing method, we first printed three samples of the same arbitrary shape, an outline of an "M" with five different curved sections (Figure 3). Each of these samples underwent a different shape-programming procedure. In the first (top of Figure 3, Movie S1), we programmed a spiral into the printed structure by cutting the sample and wrapping it around a rod multiple times during shape programming. The resulting LCE transitioned

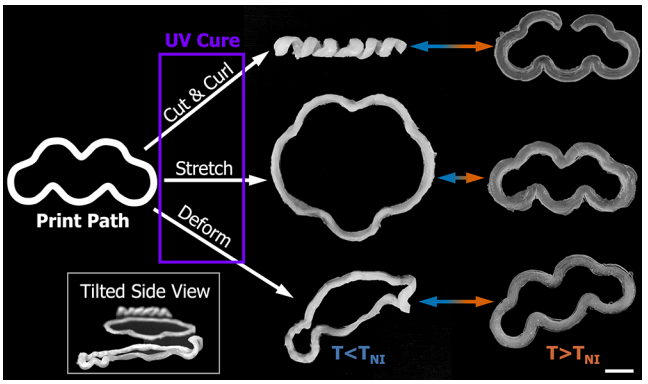

Figure 3. Photographs of LCE samples demonstrating variety of deformations that can be programmed from the same initial printed structure. Three different LCEs were produced using the same print path (in the shape of an "M") followed by different shape programming steps. The LCE shown at the top was cut and curled around a rod during shape programming. The LCE shown in the middle was stretched radially outward for shape programming. The LCE shown at the bottom was shape-programmed by creating a sinusoidal wave shape, eliminating the divot between the top two curves, curling the right curve around a cylinder and stretching the bottom curve. Scale bar is 1 cm.

between the spiral structure and the original "M" shape upon cooling to room temperature and heating to ~120 °C, respectively. In the second sample (middle of Figure 3, Movie S2), we stretched the printed structure radially outward during shape programming to create a more circular shape. This sample reversibly transitioned between the more open structure and the original "M" shape. In the last sample, demonstrated multiple deformations were programmed into a single material (bottom of Figure 3, Movie S3). We created a sinusoidal wave on the left curved section, straightened the curves between two top curved sections, curled the right curved section, and uniaxially stretched the bottom curved section of the "M". This sample also reversibly transitioned between the shape defined during shape programming and the initial "M" shape. These examples demonstrate how our method can take a single printed structure and shape-program virtually arbitrary shape changes. No mathematical determination of the director profile was needed to program these shape changes, allowing for the rapid fabrication of the arbitrary shape changes.

To further demonstrate the shapes and shape changes possible with our 3D printing technique, we printed and shape-programmed circular LCEs, auxetic honeycomb LCEs, and flat LCE films with divots that appear on cooling. Figure 4a,b shows two multilayer (12 layers) circular LCE structures printed using the same print path. The first circular structure was stretched and curled to create a shape at room temperature that was circular from a side view and square from a top view, and the second was curled around three consecutive rods to create a wave shape. Both LCEs ultimately transformed between the programmed shape and printed circle when cooled and heated, respectively (Figure 4a,b, Supporting Information Movies S4 and S5). We also printed a honeycomb structure that was stretched biaxially and shape-programmed to create an auxetic shape-shifting material (Figure 4c, Supporting Information Movie S6).

Our 3D-printing approach also enables programming symmetry-breaking shape changes in LCE samples. To

https://dx.doi.org/10.1021/acsami.0c07331
ACS Appl. Mater. Interfaces 2020, 12, 28692−28699

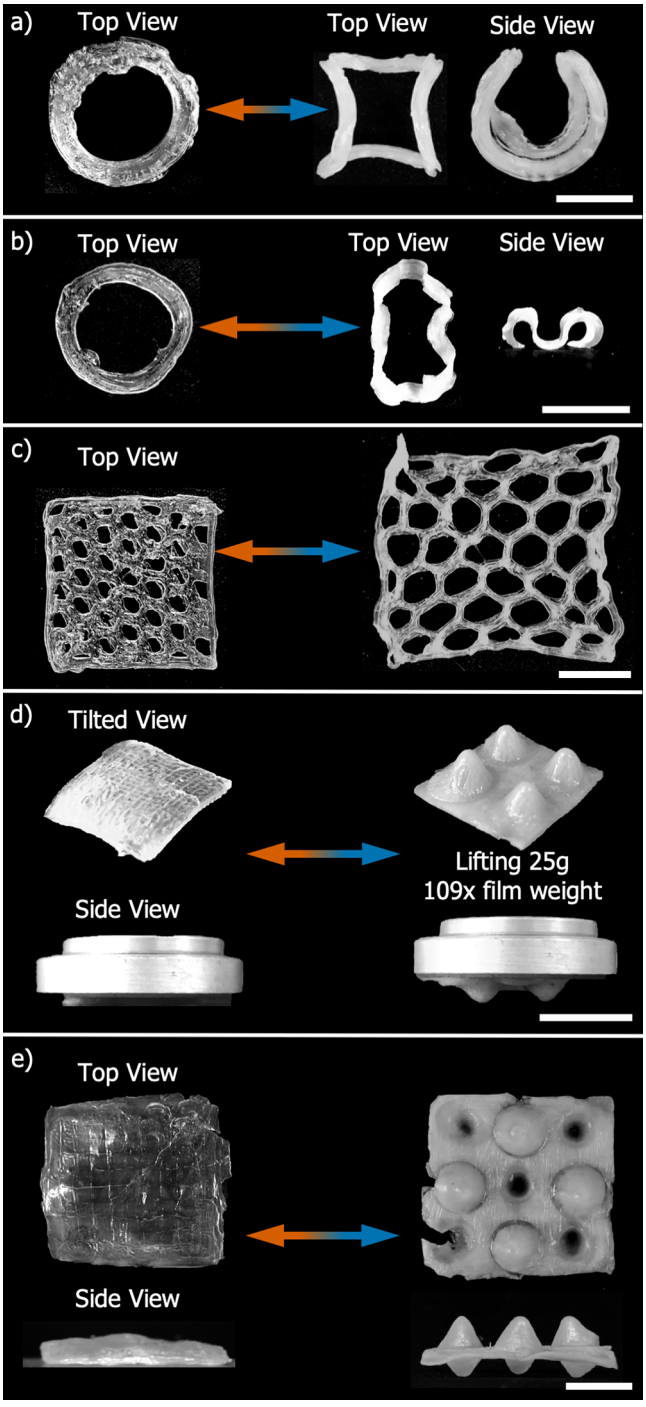

Figure 4. Photographs of multilayered 4D printed LCE samples, auxetic LCEs, and symmetry breaking in 4D printed samples. Twelve-layer-printed LCE cylinders are programmed to (a) stretch and curl or (b) produce a wave-like structure. (c) LCE that undergoes a reversible auxetic shape-change. (d,e) Example of symmetry breaking in LCE samples that transition between a flat sheet and a sheet with peaks emerging in either direction out of the film. The peaks can be programmed to emerge, all pointing in the same direction (d) or point in different directions; (e) scale bars are 1 cm.

demonstrate this, we printed a flat LCE sheet which we then deformed by pressing a sharp stick into the film to create cone-shaped peaks. On cooling, the peaks emerged from one side of the flat film and could lift a 25 g weight to a height of almost 5 mm, which corresponds to a specific work of 4 J/kg (Figure 4d, Supporting Information Movie S7). This shape is similar to the "+1 point defect" used to create cones in other reported LCEs,[26,27] but our method allows us to break sample symmetry and easily program the "defects" to controllably pop upward or downward out of the film. We further demonstrate this in Figure 4e and Supporting Information Movie S8. In this structure, we created four large peaks that came upward out of the film and five smaller peaks emerged downward out of the film. The final structure seamlessly combines these features with regions that do not change shape.

CONCLUSIONS

We demonstrated a reactive 3D printing method for LCEs that enabled straightforward programming of complex shape changes in printed soft actuators. The method involved printing into a reactive catalyst bath followed by shape programming, and the resulting LCEs could reversibly shape-shift between the printed and shape-programmed architectures when heating and cooling, respectively. We demonstrated the versatility of printable soft actuators by programming a variety of shape changes previously unobtainable by traditional printing methods, such as auxetic LCEs, symmetry breaking in LCEs, and different shape changes programmed in LCEs prepared using the same print path. This method will be useful in the development of LCE actuators with complex architectures and shape changes. A current limitation of this printing process is the inability to create structures with unsupported printed fibers. All printed structures have to be printed layer-by-layer onto a hard surface. However, further optimization of the reaction kinetics, such as increasing the catalyst concentration in the bath, could provide pathways to enable printed fibers that gel rapidly enough to be self-supporting during the printing process. Additionally, scaffold-assisted 3D printed designs, where a specific print path may be required, will be useful for developing complex shapes changes using this method. In short, reactive 3D printing of LCEs will open opportunities for architectural freedom and virtually arbitrary shape changes in soft robotic systems.

ASSOCIATED CONTENT

Supporting Information

The Supporting Information is available free of charge at https://pubs.acs.org/doi/10.1021/acsami.0c07331.

Additional LCE characterization including rheological analysis, dynamic scanning calorimetry, and swelling studies (PDF)

Movies demonstrating actuation in 3D printed LCE samples; reversible actuation of a spiral turning into an "M" architecture (AVI)

Reversible actuation of a circular flower outline into an "M" architecture (AVI)

Reversible actuation of an arbitrary shape turning into an "M" architecture (AVI)

Reversible actuation of a cylinder/square architecture turning into a circle (AVI)

Reversible actuation of a curled side-view "M" architecture turning into a circle (AVI)

Reversible actuation of an auxetic honeycomb architecture (AVI)

Reversible actuation of a four-pillar LCE lifting a 25 g weight (AVI)

https://dx.doi.org/10.1021/acsami.0c07331
ACS Appl. Mater. Interfaces 2020, 12, 28692−28699

Reversible actuation of a multipeaked structure turning into a flat object (AVI)

AUTHOR INFORMATION

Corresponding Authors

Muhammad M. Rahman − *Department of Materials Science and NanoEngineering, Rice University, Houston, Texas 77005, United States;* orcid.org/0000-0003-1374-0561; Email: mr64@rice.edu

Pulickel M. Ajayan − *Department of Materials Science and NanoEngineering, Rice University, Houston, Texas 77005, United States;* orcid.org/0000-0001-8323-7860; Email: ajayan@rice.edu

Rafael Verduzco − *Department of Materials Science and NanoEngineering and Department of Chemical and Biomolecular Engineering, Rice University, Houston, Texas 77005, United States;* orcid.org/0000-0002-3649-3455; Email: rafaelv@rice.edu

Authors

Morgan Barnes − *Department of Materials Science and NanoEngineering, Rice University, Houston, Texas 77005, United States*

Seyed M. Sajadi − *Department of Materials Science and NanoEngineering, Rice University, Houston, Texas 77005, United States*

Shaan Parekh − *Department of Chemical and Biomolecular Engineering, Rice University, Houston, Texas 77005, United States*

Complete contact information is available at: https://pubs.acs.org/10.1021/acsami.0c07331

Author Contributions

M.B., M.M.R., P.M.A., and R.V. conceived the idea and led the project, M.B and S.P. conducted chemistry optimization and material characterization, S.M.S. operated the 3D printer, and M.B, M.M.R., and R.V. wrote the manuscript.

Notes

The authors declare no competing financial interest.

ACKNOWLEDGMENTS

The authors acknowledge support from the Shared Equipment Authority at Rice University, the Welch Foundation for Chemical Research (C-1888), and the Army Research Office Chemical Sciences Division (W911NF1810289).

REFERENCES

(1) Zeng, H.; Wasylczyk, P.; Parmeggiani, C.; Martella, D.; Burresi, M.; Wiersma, D. S. Light-Fueled Microscopic Walkers. *Adv. Mater.* **2015**, *27*, 3883−3887.

(2) Saed, M. O.; Ambulo, C. P.; Kim, H.; De, R.; Raval, V.; Searles, K.; Siddiqui, D. A.; Cue, J. M. O.; Stefan, M. C.; Shankar, M. R.; Ware, T. H. Molecularly-Engineered, 4D-Printed Liquid Crystal Elastomer Actuators. *Adv. Funct. Mater.* **2018**, *29*, 1806412.

(3) Ambulo, C. P.; Burroughs, J. J.; Boothby, J. M.; Kim, H.; Shankar, M. R.; Ware, T. H. Four-Dimensional Printing of Liquid Crystal Elastomers. *ACS Appl. Mater. Interfaces* **2017**, *9*, 37332−37339.

(4) Kotikian, A.; Truby, R. L.; Boley, J. W.; White, T. J.; Lewis, J. A. 3D Printing of Liquid Crystal Elastomeric Actuators with Spatially Programed Nematic Order. *Adv. Mater.* **2018**, *30*, 1706164.

(5) Wehner, M.; Truby, R. L.; Fitzgerald, D. J.; Mosadegh, B.; Whitesides, G. M.; Lewis, J. A.; Wood, R. J. An Integrated Design and Fabrication Strategy for Entirely Soft, Autonomous Robots. *Nature* **2016**, *536*, 451−455.

(6) Compton, B. G.; Lewis, J. A. 3D-Printing of Lightweight Cellular Composites. *Adv. Mater.* **2014**, *26*, 5930−5935.

(7) Kuang, X.; Roach, D. J.; Wu, J.; Hamel, C. M.; Ding, Z.; Wang, T.; Dunn, M. L.; Qi, H. J. Advances in 4D Printing: Materials and Applications. *Adv. Funct. Mater.* **2019**, *29*, 1805290.

(8) Morimoto, Y.; Onoe, H.; Takeuchi, S. Biohybrid Robot Powered by an Antagonistic Pair of Skeletal Muscle Tissues. *Sci. Rob.* **2018**, *3*, No. eaat4440.

(9) López-Valdeolivas, M.; Liu, D.; Broer, D. J.; Sánchez-Somolinos, C. 4D Printed Actuators with Soft-Robotic Functions. *Macromol. Rapid Commun.* **2018**, *39*, 1700710.

(10) Sydney Gladman, A.; Matsumoto, E. A.; Nuzzo, R. G.; Mahadevan, L.; Lewis, J. A. Biomimetic 4D Printing. *Nat. Mater.* **2016**, *15*, 413−418.

(11) Wu, J.; Yuan, C.; Ding, Z.; Isakov, M.; Mao, Y.; Wang, T.; Dunn, M. L.; Qi, H. J. Multi-Shape Active Composites by 3D Printing of Digital Shape Memory Polymers. *Sci. Rep.* **2016**, *6*, 24224.

(12) Ge, Q.; Sakhaei, A. H.; Lee, H.; Dunn, C. K.; Fang, N. X.; Dunn, M. L. Multimaterial 4D Printing with Tailorable Shape Memory Polymers. *Sci. Rep.* **2016**, *6*, 31110.

(13) Mao, Y.; Ding, Z.; Yuan, C.; Ai, S.; Isakov, M.; Wu, J.; Wang, T.; Dunn, M. L.; Jerry Qi, H. 3D Printed Reversible Shape Changing Components with Stimuli Responsive Materials. *Sci. Rep.* **2016**, *6*, 24761.

(14) Wu, J.; Zhao, Z.; Kuang, X.; Hamel, C. M.; Fang, D.; Qi, H. J. Reversible Shape Change Structures by Grayscale Pattern 4D Printing. *Multifunct. Mater.* **2018**, *1*, 015002.

(15) Boley, J. W.; Van Rees, W. M.; Lissandrello, C.; Horenstein, M. N.; Truby, R. L.; Kotikian, A.; Lewis, J. A.; Mahadevan, L. Shape-Shifting Structured Lattices via Multimaterial 4D Printing. *Proc. Natl. Acad. Sci. U.S.A.* **2019**, *116*, 20856−20862.

(16) Naficy, S.; Gately, R.; Gorkin, R.; Xin, H.; Spinks, G. M. 4D Printing of Reversible Shape Morphing Hydrogel Structures. *Macromol. Mater. Eng.* **2017**, *302*, 1600212.

(17) Aharoni, H.; Sharon, E.; Kupferman, R. Geometry of Thin Nematic Elastomer Sheets. *Phys. Rev. Lett.* **2014**, *113*, 257801.

(18) Roach, D. J.; Kuang, X.; Yuan, C.; Chen, K.; Qi, H. J. Novel Ink for Ambient Condition Printing of Liquid Crystal Elastomers for 4D Printing. *Smart Mater. Struct.* **2018**, *27*, 125011.

(19) Davidson, E. C.; Kotikian, A.; Li, S.; Aizenberg, J.; Lewis, J. A. 3D Printable and Reconfigurable Liquid Crystal Elastomers with Light-Induced Shape Memory via Dynamic Bond Exchange. *Adv. Mater.* **2020**, *32*, 1905682.

(20) Warner, M.; Terentjev, E. M. *Liquid Crystal Elastomers*; Oxford University Press: Oxford, England, 2003.

(21) Agrawal, A.; Chen, H.; Kim, H.; Zhu, B.; Adetiba, O.; Miranda, A.; Cristian Chipara, A.; Ajayan, P. M.; Jacot, J. G.; Verduzco, R. Electromechanically Responsive Liquid Crystal Elastomer Nanocomposites for Active Cell Culture. *ACS Macro Lett.* **2016**, *5*, 1386−1390.

(22) Wang, C.; Sim, K.; Chen, J.; Kim, H.; Rao, Z.; Li, Y.; Chen, W.; Song, J.; Verduzco, R.; Yu, C. Soft Ultrathin Electronics Innervated Adaptive Fully Soft Robots. *Adv. Mater.* **2018**, *30*, 1706695.

(23) Wani, O. M.; Zeng, H.; Priimagi, A. A Light-Driven Artificial Flytrap. *Nat. Commun.* **2017**, *8*, 15546.

(24) Tian, H.; Wang, Z.; Chen, Y.; Shao, J.; Gao, T.; Cai, S. Polydopamine-Coated Main-Chain Liquid Crystal Elastomer as Optically Driven Artificial Muscle. *ACS Appl. Mater. Interfaces* **2018**, *10*, 8307−8316.

(25) Brannum, M. T.; Steele, A. M.; Venetos, M. C.; Korley, L. T. J.; Wnek, G. E.; White, T. J. Light Control with Liquid Crystalline Elastomers. *Adv. Opt. Mater.* **2019**, *7*, 1801683.

(26) Ware, T. H.; McConney, M. E.; Wie, J. J.; Tondiglia, V. P.; White, T. J. Voxelated Liquid Crystal Elastomers. *Science* **2015**, *347*, 982−984.

(27) Ahn, S.-k.; Ware, T. H.; Lee, K. M.; Tondiglia, V. P.; White, T. J. Photoinduced Topographical Feature Development in Blueprinted

Azobenzene-Functionalized Liquid Crystalline Elastomers. *Adv. Funct. Mater.* **2016**, *26*, 5819−5826.
(28) Zeng, H.; Wani, O. M.; Wasylczyk, P.; Kaczmarek, R.; Priimagi, A. Self-Regulating Iris Based on Light-Actuated Liquid Crystal Elastomer. *Adv. Mater.* **2017**, *29*, 1701814.
(29) Agrawal, A.; Adetiba, O.; Kim, H.; Chen, H.; Jacot, J. G.; Verduzco, R. Stimuli-Responsive Liquid Crystal Elastomers for Dynamic Cell Culture. *J. Mater. Res.* **2015**, *30*, 453−462.
(30) Pei, Z.; Yang, Y.; Chen, Q.; Terentjev, E. M.; Wei, Y.; Ji, Y. Mouldable Liquid-Crystalline Elastomer Actuators with Exchangeable Covalent Bonds. *Nat. Mater.* **2014**, *13*, 36−41.
(31) Barnes, M.; Verduzco, R. Direct Shape Programming of Liquid Crystal Elastomers. *Soft Matter* **2019**, *15*, 870−879.
(32) White, T. J.; Broer, D. J. Programmable and Adaptive Mechanics with Liquid Crystal Polymer Networks and Elastomers. *Nat. Mater.* **2015**, *14*, 1087−1098.
(33) Yakacki, C. M.; Saed, M.; Nair, D. P.; Gong, T.; Reed, S. M.; Bowman, C. N. Tailorable and Programmable Liquid-Crystalline Elastomers Using a Two-Stage Thiol−Acrylate Reaction. *RSC Adv.* **2015**, *5*, 18997−19001.
(34) Chan, J. W.; Hoyle, C. E.; Lowe, A. B.; Bowman, M. Nucleophile-Initiated Thiol-Michael Reactions: Effect of Organocatalyst, Thiol, and Ene. *Macromolecules* **2010**, *43*, 6381−6388.
(35) Torrado, A. R.; Shemelya, C. M.; English, J. D.; Lin, Y.; Wicker, R. B.; Roberson, D. A. Characterizing the Effect of Additives to ABS on the Mechanical Property Anisotropy of Specimens Fabricated by Material Extrusion 3D Printing. *Addit. Manuf.* **2015**, *6*, 16−29.
(36) Es-Said, O. S.; Foyos, J.; Noorani, R.; Mendelson, M.; Marloth, R.; Pregger, B. A. Effect of Layer Orientation on Mechanical Properties of Rapid Prototyped Samples. *Mater. Manuf. Processes* **2000**, *15*, 107−122.
(37) Shaffer, S.; Yang, K.; Vargas, J.; Di Prima, M. A.; Voit, W. On Reducing Anisotropy in 3D Printed Polymers via Ionizing Radiation. *Polymer* **2014**, *55*, 5969−5979.
(38) Ware, T. H.; Biggins, J. S.; Shick, A. F.; Warner, M.; White, T. J. Localized Soft Elasticity in Liquid Crystal Elastomers. *Nat. Commun.* **2016**, *7*, 10781.
(39) Dey, S.; Agra-Kooijman, D.; Ren, W.; McMullan, P.; Kumar, S.; Griffin, A. Soft Elasticity in Main Chain Liquid Crystal Elastomers. *Crystals* **2013**, *3*, 363−390.

https://dx.doi.org/10.1021/acsami.0c07331
ACS Appl. Mater. Interfaces 2020, 12, 28692−28699